https://dx.doi.org/10.1016/j.nanoen.2020.105117

Predicting Performance of Fiber Thermoelectric Generator Arrays in Wearable Electronic Applications

Li-sha Zhang [a], Bao Yang [a], Shu-pin Lin [a], Tao Hua [a], Xiao-ming Tao [a]*

[a] Research Center of Smart Wearable Technology, Institute of Textiles and Clothing, The Hong Kong Polytechnic University, Hong Kong, P.R. China

**xiao-ming.tao@polyu.edu.hk*

Abstract

Emerging fiber-based thermoelectric generators have shown great potentials to power wearable electronics by harvesting thermal energy from human body and environment. However, the lack of quantitative analytical tools has hindered the research progress, particularly related to their design and evaluation, covering selection and optimization of thermoelectric, electric and structural materials, device structure, fabrication processes and application conditions. Here, we report a quantitative approach to predict the performance of three-dimensional fiber-based thermoelectric generators composed of one-dimensional fiber generator array, working under conductive and radiative heat transfer conditions with a low temperature difference. We first present an experimentally verified model of single fiber generator unit, consisting of core/sheath fiber leg and electrodes, to quantify the effects of the material properties and structural parameters on the output power and energy conversion efficiency of the fiber unit. Then we propose a second model of three-dimensional fiber-based thermoelectric array generator to predict its output performance in terms of fiber unit packing density and surface emissivity. Finally, the theoretical upper limits of output power and conversion efficiency are given for the fiber-based thermoelectric array generators worn on a human torso back under a range of ambient temperature.

Keywords: Fiber-based thermoelectric generator array; Power; Energy conversion efficiency; Conduction and radiation; Geometric parameters; wearable application.

Nomenclature

Abbreviations

TEG	Thermoelectric generator
FTEG	Fiber-based thermoelectric generator

Symbols

$\boldsymbol{A}$	Surface area of the body (m^2)
$\boldsymbol{I}$	Current (A)
$\boldsymbol{K}$	thermal conductance (W/K)
$\boldsymbol{L}$	Length of TE leg (m)
$\boldsymbol{P}$	Output power (W)
$\boldsymbol{q}$	Heat rate (W)
$\boldsymbol{r}$	Radius (m)
$\boldsymbol{R}$	Electrical resistance (Ω)
$\boldsymbol{T}$	Temperature (K)
$\Delta\boldsymbol{T}$	Temperature difference (K)
$\boldsymbol{U}$	Voltage (V)

Subscripts

$\boldsymbol{c}$	Cold
$\boldsymbol{ex}$	External
$\boldsymbol{f}$	Fiber
$\boldsymbol{h}$	Hot
$\boldsymbol{in}$	Flow into
$\boldsymbol{max}$	Maximum
$\boldsymbol{rad}$	Radiation
$\boldsymbol{s}$	Body surface
$\boldsymbol{sur}$	Surroundings
$\boldsymbol{tot}$	Total
$\boldsymbol{TE}$	Thermoelectric material

Greek letters

$\boldsymbol{\alpha}$	Seebeck coefficient (V/K)
$\boldsymbol{\delta}$	Thickness of TE layer (m)
$\boldsymbol{\varepsilon}$	Emissivity (1)

$\boldsymbol{\eta}$	Efficiency
$\boldsymbol{\rho}$	Electrical resistivity (Ω/m)
$\boldsymbol{\sigma}$	Electrical conductivity (S/m)
$\boldsymbol{\sigma_{SB}}$	Stefan-Boltzmann constant, $5.670 \times 10^{-8}\ \mathrm{W/(m^2 \cdot K^4)}$

1 Introduction

Fiber-based thermoelectric generators (FTEGs) are flexible, conformable and light-weight devices, which can directly convert heat into electricity without any moving parts or working fluids [1]. At present, the output performance of such devices is generally lower, in the range of ~1 $\mu W/cm^2$, close to body temperature with a small temperature difference, say ~15 K [2, 3]. These devices are great candidates to provide energy to the wearable electronics. To this end, high output power and energy conversion efficient are essential for FTEGs in wearable applications. However, up to date, there is no quantitative analytical tool that can guide the engineering design of FTEGs, including selection of thermoelectric (TE), electric and structural materials, the device structure and fabrication processes with particular application conditions.

To achieve high energy conversion efficiency of rigid thermoelectric generators (TEGs), significant progress has been made to explore TE materials of high figure of merit , $ZT = \sigma\alpha^2 T/\kappa$, where σ is the electrical conductivity; α is the Seebeck coefficient; T is the temperature; κ is the thermal conductivity [4-9]. For the power generation application, these materials include Bi_2Te_3 and its alloy [10], silicides [11], PbTe [12-14], half-Heusler [15], poly(3,4-ethylenedioxythiophene): poly(styrenesulfonate) (PEDOT: PSS) [16], and graphene and composites [17]. The theoretical studies of traditional TEGs have been conducted for solid cuboid structure, usually with a large temperature difference and under conditions of conductive heat transfer [18-20]. These models have provided important engineering design guidelines in

traditional rigid TEGs by changing the cross-sectional area, length and segment of solid p- and n-type TE legs for the high output performance [21-24]. However, these models cannot be applied in the wearable applications where the temperature at one end is fixed but at the other end is free. For example, the surface temperature of human torso can be regarded as a constant. Under this condition, the temperature at the other end is the result of the heat transfer.

Three-dimensional (3D) spacer fabric structure may offer high specific output power from the FTEGs because of the light weight and the large temperature difference between the face and back sides connected by numerous one-dimensional (1D) FTEG units[1]. The output performance of the 3D FTEGs is determined by those of 1D FTEGs. Compared with the thick TE columns in traditional rigid TEG arrays, the 1D FTEG units have much higher aspect ratio, which results in the large deformability and flexibility. A recent work reported 3D space fabric FTEGs comprising 1D FTEG units where the core was a carbon nanotube yarn (CNTY) acting as a continuous electrode[3]. The sheath was coated with p-type PEDOT: PSS and n-type polyethyleneimine (PEI). It is not desirable that in the FTEGs much thermal energy was conducted from the hot to cold end through the CNTY of high thermal conductivity. Therefore, higher performance of the FTEG can be achieved with a more appropriate consideration of materials and device structure, ideally guided by a quantitative analytical tool.

Hence, this paper presents a quantitative approach to predict the performance of 3D FTEG composed of 1D FTEG array in simulated wearable conditions, that is, under conductive and radiative heat transfer with low temperature differences. The single 1D FTEG unit, consisting of core/sheath fiber TEG leg and electrodes, is dealt with under conduction and radiation heat transfer. The influences of the radius and the length of filament, the thickness of TE coating layer, the

distance between the adjacent surfaces of 1D FTEGs and the surface emissivity are quantified. Finally, the upper limits of output power and conversion efficiency of the FTEG array device with various TE materials are given if worn on a human torso back under a range of ambient temperature.

2 Models and experimental verification

2.1 Mathematical model

FTEG devices convert thermal energy into electrical energy according to the Seebeck effect. Fig. 1(a) illustrates a 1D FTEG unit comprising a polymer core filament coated with TE material in the middle and conductive material at its both ends. Based on the Seebeck effect, the equivalent voltage source, *U*, induced by the temperature difference can be estimated by the following equation

$$U = \alpha \cdot \Delta T \tag{1}$$

where α is the Seebeck coefficient of TE material, ΔT is the temperature difference between the hot and cold ends. Therefore, two factors directly affect the generated electrical potential: the material property and the temperature difference. For the same material, the temperature distribution along the thermal conduction direction is the pivot of the potential. To study this factor, the model of 1D FTEG was investigated under the conductive and radiative heat transfer, as shown in Fig. 1(a). Meanwhile, the model under the only conductive heat transfer was a special case, which was studied at first (**Supplementary materials S1.1**).

Several initial assumptions are made: (1) The thickness of the electrode is ultrathin as compared with the radius of fiber. Thus, the temperature field of the electrode is the same as that of the connected end of the TE fiber. Meanwhile, the lateral heat dissipation from the electrode

can be neglected. (2) The heat transfer from the electrode to the connected wire is neglected due to the small cross-section of the wire. (3) The temperature field of each cross-section of the electrode and the TE fiber is uniform. (4) The interface between the TE material and electrodes is treated in two scenarios, that is, with and without the thermal and electrical contact resistance. For the derivation of theoretical upper limits for the output, the ideal scenario without contact resistant is presented in the main body and the other scenario, the treatment is presented in **Supplementary materials S2** (5) The convective heat transfer is not considered. (6) The surface of 1D FTEG was opaque, diffuse and grey.

The radiative heat rate can be given by the following expression:

$$q_{rad} = \sigma_{SB} \varepsilon A_s (T_s^4 - T_{sur}^4) \tag{2}$$

where σ_{SB} is the Stefan-Boltzmann constant, $5.670 \times 10^{-8}\ \mathrm{W/(m^2 \cdot K^4)}$; ε is the emissivity; T_s is the surface temperature of the TE leg; T_{sur} is the temperature of the surroundings; A_s is the surface area of the body. Based on the Kirchhoff law, the current through the external resistance is given by

$$I = \frac{\alpha \cdot \Delta T}{R_{TE} + R_{ex} + R_{tot}} \tag{3}$$

where R_{ex} is the current through the external resistance; R_{tot} is the total resistance of the electrodes, the wires and the connection between them. R_{TE} is the resistance of the TE fiber, which is given by

$$R_{TE} = \rho_{TE} \frac{L}{\pi[(r_f + \delta)^2 - {r_f}^2]} \tag{4}$$

where ρ_{TE} is the electrical resistivity of TE material; L and d are the length and thickness of the TE layer, respectively; r_f is the radius of the filament.

Then, the output power is the current through the electric potential between the two ends of the external resistance, which can be given by

$$P = I^2 R_{ex} \tag{5}$$

When $R_{ex} = R_{tot} + R_{TE}$, there is the maximum of output power, P_{max}.

From Eqn. (3) and (5), ΔT has a quadratic (the highest order) effect on the output power. In this study, the thermal analysis of FTEG was firstly studied under the only conductive heat transfer. The temperature at the hot and cold ends were constants. Then, the analysis was investigated under the conductive and radiative heat transfer. The temperature at the hot end was still a constant. But at the cold end, the temperature was the result of the heat transfer, which was not a constant.

The heat rate input (q_{in}) at the high temperature end can be described with the following expression:

$$q_{in} = \alpha T_h I + K_{tot}(T_h - T_c) - \frac{1}{2} I^2 R_{TE} - q_{rad} \tag{6}$$

where K_{tot} is the total thermal conductance. The efficiency of the thermoelectric generator system, η, is the ratio of the output power and the heat rate input, which can be given by

$$\eta = \frac{P}{q_{in}} \tag{7}$$

The maximum of efficiency, η_{max}, is defined as the efficiency under the condition that the output power reaches the maximum, $P = P_{max}$.

Based on the above assumptions and governing equations, the temperature distribution of 1D FTEG along the conductive heat transfer can only be expressed in an implicit solution, rather than an analytical solution (**Supplementary materials S1.2**). But the numerical analysis can be a powerful method to depict this distribution and temperature difference. Thus, the performance of the device can be predicted. The numerical solution of single 1D FTEG and its array is studied in the following part.

2.2 Numerical simulations

Under the only conduction situation, the single 1D FTEG model had fixed-fixed temperature at two ends, which were specified as 100 ℃ and 25 ℃. All models in this research were studied at steady-state, without the variation of mass or specific heat capacitance. The numerical solution was obtained with COMSOL Multiphysics®. The geometric parameters were changed to identify the importance of factors in the performance of 1D FTEG. As the diameter of natural fiber is in the range of 15~120 μm [25], the fiber/filament diameter in the 1D FTEG models is set in the range of 25~100 μm. That is, the radius increases from 12.5 μm to 50 μm in the step length of 12.5. Additionally, in the previously reported flexible TEGs, the thickness of TE legs is in the range of 0.1~150 μm [26-33]. Thus, in the models, the range of thickness of TE legs is from 0.01 to 100 μm, which increments with one order of magnitude. The thickness of 0.01 μm is investigated to explain the unnecessary of the fabrication of ultra-thin TE layer. Besides, based on the past studies

about numerical simulation, the height of TE legs is in the range of 0.01~100 mm[34-39]. In the simulation, Bi_2Te_3 [5] is used as the TE material at first, whose properties are in the range of the Bi_2Te_3 and its alloy from other research groups, according to the latest review article [40]. Other TE materials is applied in the study of Section 4. The properties of materials are shown in Table 1.

One of the significant advantages of 1D FTEGs is its flexibility due to its slenderness. Based on this property, an important potential application is that 1D FTEGs are fabricated into space fabrics to form flexible devices, as shown in Fig. 1(b). Four single 1D FTEGs constituted a 3D FTEG unit. In order to study the influence of the distance between 1D FTEGs on the device's performance, a model is designed and investigated, as shown in Fig. 1(c). This distance reflects the density of arrangement of the 1D FTEGs, which is known as the filling factor. The whole device is supposed to be infinite large, which is composed of large number of repeating units in the *x*-*y* plane. The fabric electrodes and conductive yarns in Fig. 1(b) are simplified as the top and bottom electrode plates in Fig. 1(c). The distance between the adjacent 1D FTEGs is given by

$$\Delta \mathrm{r} = \mathrm{c} \cdot (r_f + \delta) \tag{8}$$

where c is a controlled parameter, increasing from 1 to 3 with a step-length of 0.5. In this unit structure, the distance between the surface of 1D FTEGs and the edge of the electrode is Δr/2. The radius of filament (r_f) and thickness of TE layer (δ) were set as 12.5 μm and 10 μm, respectively, in this model. If the FTEG device comprises only one type of TE materials, the appropriate approach to connect TE legs is to design the device in Ⅱ-structure (**Supplementary material S3**). Therefore, the array unit of 1D FTEG is a 2×2 matrix structure in Fig. 1(c).

2.3 Experimental verification of single 1D FTEG under conductive heat transfer

The numerical solution of single 1D FTEG under only conductive heat transfer can be found in **Supplementary material Fig. S4.** The shorter the 1D FTEG, the larger the output power. In addition, the increment of the thickness of TE layer increases the output power in orders of magnitude. To verify this solution, 1D FTEG was fabricated with the polyester (PET) filament as the substrate, and the PEDOT: PSS as the TE material (**Supplementary material S5.1**). The thermoelectric properties and the thermo-gravimetric analysis (TGA) of PEDOT: PSS was measured and characterized in **Fig. S5** and **Fig. S6**, respectively. Besides, the morphologies of the original PET filament and 4-layer PEDOT: PSS coated filament are obtained by SEM, as illustrated in Fig. 1(d) and (e). Compared with the original PET filament, the coated one is smooth and uniform. Additionally, Fig. 1(f) illustrates the almost linearly relationship between the thickness of coating layer and the number of layers. The detailed data can be found in **Table S5.** The electrical potential of these 1D FTEGs is measured with the lab-made measurement system (**Supplementary material S5.4**). As shown in Fig. 1(f), the electrical potential is fluctuated around 1.00 mV, although the number of coating layers increases and the thickness of PEDOT: PSS increments. This is the result of the unchanged Seebeck coefficient and temperature difference, based on Eqn. (1). Besides, under only conductive heat transfer, the numerical solution of single 1D FTEG model is 1.04 mV for all cases in Fig. 1(f). From the experimental results, the electrical potential is 1.02 mV when the PET filament is coated PEDOT: PSS with 8 or 10 layers, which approaches to the numerical solution with only around 2% of difference. This result indicates that the variation of thickness in the same order of magnitude has little influence on the potential. The fabrication with these materials can be conducted by coating 8 layers. The increment of coating layers is possible to lead to poor performance, instead of the desired increase of electrical potential.

As the temperature range is $296\sim361\,\mathrm{K}$, the electrical conductivity is around $675\,\mathrm{S\cdot m^{-1}}$. Therefore, the resistance of TE layer can be calculated, according to the law of resistance. For samples with different coating layers, the internal resistance, experimental and numerical maximum output power can be obtained (Fig. 1(g)). Although the increase of coating layers little facilitates the improvement of electrical potential (Fig. 1(f)), the increment of layer thickness does reduce the internal resistance (Fig. 1(g)). Therefore, the lines of the maximum of output power gradually climbs up. Due to the fluctuation of electrical potential, the experimental results of the maximum of output power is not exactly linear. In the same fashion, the numerical results of maximum of output power increase with a constant slope rate. In addition, when the filaments are coated with 4 and 15 layers, the thickness of TE material exhibits one order of magnitude difference. This difference leads to almost one order of magnitude difference of the numerical results of the maximum of output power. This is in accordance with the results in the former discussion: the different orders of magnitude of TE material thickness causes the different orders of magnitude of maximum output power.

3 Influencing factors on performance of 1D FTEG array

In this section, for quantifying the importance of factors, the single 1D FTEG is studied under conductive and radiative heat transfer at first. Then, the 1D FTEG array formed by the single ones is investigated with the consideration of the influence of the controlled parameter.

3.1 Single 1D FTEG under conductive and radiative heat transfer

Based on the above verified model, the numerical solution was used to study the influence of geometric parameters on the performance of 1D FTEG in the fixed-free ends situation. In this situation, the temperature at the hot end was fixed at $100\,℃$. And at the free end, it was the result

of the conductive and radiative heat transfer. As known from the former part investigation, the thickness of TE layer is the primary factor on the maximum of output power of single 1D FTEG. It was 1 μm, 10 μm and 100 μm in this part study. The radius of fiber and the length of TE layer were 12.5 μm and 1 mm, respectively, which were unchanged.

To focus on the investigation of the influence of geometric parameters on the performance, the emissivity of TE material is set as 0.5 in Fig. 2 (a) and (b). The curves can be divided into three groups, according to the thickness of TE layer. The thicker the TE layer is, the higher the maximum of power is. However, the efficiency does not simply increase with the increment of the thickness. The higher efficiency occurs when the thickness of TE layer of 10 μm, for the same fiber radius. Especially, the highest efficiency is from the model with the fiber radius of 12.5 μm. This phenomenon is the result of the synergy of the conduction and radiation heat transfer, as depicted in Fig. 2(c). For the fiber radius of 12.5 μm, if the thickness of TE layer increases, the maximum of efficiency dramatically increments then gradually decrements, which reaches the peak at the thickness of 10 μm. When the thickness is smaller than 10 μm, compared with the heat loss due to the radiation, the primary effect of the increment of the thickness is the increased power. However, when the thickness is larger than 10 μm, the major effect is the conductive and radiative heat transfer through the TE material leading to the rise of the temperature at the cold end and the decrease of the temperature difference (**Supplementary materials Fig. S7**). As the thermal conductivity of TE material is much higher than that of the fiber, heat energy can be more easily transport to the cold end, when the thickness of TE layer is over 10 μm. This results the temperature at cold end is about 90 ℃ for the thickness of 100 μm. Thus, the temperature difference is only around 10 ℃. Additionally, the larger surface area of TE layer allows more heat energy transmitting to the ambient (**Supplementary materials Eqn. (S17)**). Thus, in the following study,

the fiber radius and thickness of TE layer were 12.5 μm and 10 μm, respectively. To study its influence on the performance of 1D FTEG, the emissivity of TE material increased from 0.1 to 0.9. In Fig. 2(d), the difference in the orders of magnitude of the maximum of power is simultaneously determined by the TE thickness and the emissivity. Especially, the highest value occurs, when the TE thickness and emissivity are 100 μm and 0.9, respectively. Besides, for the models with same geometry, the maximum of power increases with the enlarged emissivity which leads to the lower temperature at the cold end (**Fig. S8**). Thus, based on Eqn. (5), the temperature difference and output power increment. Furthermore, Fig. 2(e) illustrates the effect of the emissivity on the efficiency of 1D FTEG. When the fiber radius and the TE thickness are fixed, the increased emissivity also enhances the efficiency. Same to Fig. 2(b), the best performance of efficiency occurs, when the fiber radius and the TE thickness are 12.5 μm and 10 μm, respectively. Therefore, if the objective is just to improve the output power, the thickness of TE layer should be as large as possible, which is the most important factor. However, if the efficiency is considered at the same time, the appropriate selection of fiber radius and thickness of TE layer is the primary thing. In addition, the modification of the surface with high emissivity can be a possible method to improve the performance.

3.2 1D FTEG array under conductive and radiative heat transfer

As shown in Fig. 1(b) and (c), when the single 1D FTEGs forms the 3D FTEG, thermal energy can be transported through electrode, filament, TE layer and air by the conduction. Meanwhile, heat transmits through leaving out of the surfaces of 1D FTEGs by the radiation. Fig. 2(f) shows the linear relationship between the temperature at free end and the emissivity for models with distinct controlled parameters, when the 1D FTEG array provides the maximum of output power. Similar to the situation in **Fig. S8**, all lines slope down with the enhanced emissivity which

leads more energy to leave the surface of TE legs through the radiative heat transfer, as depicted in Eqn. (1). Although the radiative heat rate is proportional to the difference of four times of temperature in Eqn. (2), the influence is outrageously eliminated by the Stefan-Boltzmann constant. Thus, the conductive heat transfer has a more important effect than the radiative part in the array unit. Besides, when the emissivity is same, the increase of controlled parameter rises the temperature at free end, because the thermal resistance of air layer is reduced with the increment of cross-sectional area, which can be given by

$$\theta_{air} = \frac{L}{\kappa_{air} \cdot A_{air}} = \frac{L}{\kappa_{air} \cdot \pi\{[(c+1)(r_f+\delta)]^2 - (r_f+\delta)^2\}} \tag{9}$$

where κ_{air} is the thermal conductivity of air; A_{air} is the cross-sectional area of air region, which is perpendicular to the direction of the conductive heat transfer. Thus, the reduced total thermal resistance leads to the thermal energy can be easily conducted from the hot to cold ends. Therefore, the temperature at free end is elevated. The temperature at the cold end directly determines the output power and emissivity, as shown in Fig. 2(g) and (h). In Fig. 2(g), when the controlled parameter is specified, the maximum of output power increases with the enlarged emissivity. However, when the emissivity is specified, it decreases with the increment of controlled parameter. In Fig. 2(h), for the same controlled parameter, the efficiency increasing with the enlarged emissivity is caused by the elevated output power. Besides, for the same emissivity, the efficiency decreases with the increment of controlled parameter. Except for the reduced output power, this decrement of efficiency is also caused by the increase of the thickness of air layer. Therefore, in the device of 1D FTEG array, the enlarged emissivity cannot cause the output power and efficiency to change in orders of magnitude. Besides, the controlled parameter should be small, that is, the arrangement of single 1D FTEGs should be close to each other. In addition, the comparison of the

performance of 1D FTEG single and array can be found in the **Supplementary material S6.** This model only discussed the situation that air is filled between 1D FTEGs. However, it can be extended and applied to the situation that yarns or fibers are the fillers, such as cotton and polyester.

4 Upper limit of performance of array devices

Suppose the 3D FTEG composed of 1D FTEG arrays is worn on the back of a human with the surface temperature of around 35 ℃, as shown in Fig. 1(b). The ambient temperature is in the range of −55 ℃~ 55 ℃. The model in the Section 3.2 is applied to investigate the upper limit of the performance of the 1D FTEG array composed of different TE materials (in Table 1) under different ambient temperature. The control parameter and the emissivity of the 1D FTEG array are 1 and 0.5, respectively. The external resistance is equal to the internal resistance of the array (**Table S7**). Fig. 3(a) illustrates the relationship between the ambient temperature and the temperature at the free end of 1D FTEG array with different materials. As discussed in the former section, the pivot of the heat transfer is the conduction. The thermal conductivity of rGO (in Table 1) is higher one order of magnitude than others. Thus, when the ambient temperature is very low, the pink line is above the others, meaning that the temperature difference between the hot and cold end is smaller. Meanwhile, the absolute Seebeck coefficient of rGO is smaller than others. Thus, although the electrical conductivity of rGO is not the lowest, its maximum of output power is the lower than others (Fig. 3(c)). The maximum of output power is determined by the synergy of the material properties and the temperature difference. In sharp contrast to rGO, for the device composed with Ag_2Se, the maximum of output power is higher than others, when the ambient temperature is lower than 10 ℃. The large temperature difference strengthens the influence of large Seebeck coefficient of Ag_2Se on the device performance (Eqn. (3) and (5)). Corresponding to the maximum of output

power, the specific maximum of output power (**Supplementary material S7**) and the maximum of power generated by human back are also illustrated in Fig. 3(c). For a person, if the height and the weight are 168 cm and 55 kg, respectively, the surface of body is about 1.6 m^2, based on the Stevenson formula[41]. The percentage of the back is equal to that of the breast and stomach, which is about 13% the surface of body. Thus, the surface of back is about 0.208 m^2. Therefore, if the 3D FTEG composed of 1D FTEG arrays is applied to the back part of clothes, their maximum of output power is illustrated with the right outer longitudinal axis in Fig. 3(c). Thus, the 3D FTEG is a great candidate for powering glucose and blood pressure sensor, or small electronics like the Bluetooth transmitters (driving power ~5 mW; data transmission rate ~500 kbits/s; power consumption 10 nW/bit) [42]. Finally, as shown in Fig. 3(b), the tendency of efficiency is like that of the maximum of output power: the higher the output power, the higher the efficiency. For powering small wearable electronics, the output power shall be the primary consideration. In fact, by the comparison of Fig. 3(b) and (c), the improvement of output power can simultaneously increase the maximum of efficiency.

5 Conclusion

This paper reports new theoretical models for 1D FTEGs and 3D FTEG array device, working under conductive and radiative thermal transfer with a low temperature difference comparable to wearable applications, and their numerical simulation results. The influences on output power and energy conversion efficiency of the FTEGs have been given in terms of the fiber dimension, the thickness of TE coating layer, packing density of the array and the surface emissivity. The theoretical model for single 1D FTEG unit, consisting of core/sheath fiber TEG leg and electrodes, was experimentally verified with conductive thermal transfer condition. The numerical results

show that the most important factor on the output power is the thickness of TE layer in the 1D FTEG units. For the 3D FTEG array device, a lower packing density of the 1D FTEG units results in a lower output power and efficiency. Finally, the theoretical upper limits of output performance of the FTEG array device with different TE materials have been derived, for the circumstances where the device is worn on the human torso back at various ambient temperatures. For instance, an ideal 3D FTEG device with Ag_2Se as the TE material can generate a maximum power of about 0.2 W at the ambient temperature of 15 ℃. The quantitative methods proposed here can be served as engineering design and evaluation tools that will guide the research and development in a more efficient and faster manner towards the optimization of the FTEGs for wearable applications.

Acknowledgements

The work has been partially supported by Research Grants Council of Hong Kong SAR Government, China (Grant No. 15201419E, 15200917E, 15204715E) and Hong Kong Polytechnic University (Grant No. AAB3 and 847A). L.Z. acknowledges a postgraduate scholarship from the Hong Kong Polytechnic University.

References

[1] L. Zhang, S. Lin, T. Hua, B. Huang, S. Liu, X. Tao, Fiber‐Based Thermoelectric Generators: Materials, Device Structures, Fabrication, Characterization, and Applications, Advanced Energy Materials, 8 (2018) 1700524.

[2] W. Zeng, X.M. Tao, S. Lin, C. Lee, D. Shi, K.H. Lam, B. Huang, Q. Wang, Y. Zhao, Defect-engineered reduced graphene oxide sheets with high electric conductivity and controlled thermal conductivity for soft and flexible wearable thermoelectric generators, Nano Energy, 54 (2018) 163-174.

[3] Y. Zheng, Q. Zhang, W. Jin, Y. Jing, X. Chen, X. Han, Q. Bao, Y. Liu, X. Wang, S. Wang, Carbon nanotube yarn based thermoelectric textiles for harvesting thermal energy and powering electronics, J. Mater. Chem. A, DOI (2020).

[4] D. Byeon, R. Sobota, K. Delime-Codrin, S. Choi, K. Hirata, M. Adachi, M. Kiyama, T. Matsuura, Y. Yamamoto, M. Matsunami, T. Takeuchi, Discovery of colossal Seebeck effect in metallic Cu2Se, Nature Communications, 10 (2019).

[5] J.H. We, S.J. Kim, B.J. Cho, Hybrid composite of screen-printed inorganic thermoelectric film and organic conducting polymer for flexible thermoelectric power generator, Energy, 73 (2014) 506-512.

[6] J. Shi, S. Liu, L. Zhang, B. Yang, L. Shu, Y. Yang, M. Ren, Y. Wang, J. Chen, W. Chen, Y. Chai, X. Tao, Smart Textile-Integrated Microelectronic Systems for Wearable Applications, Advanced Materials, 0 (2019) 1901958.
[7] Y. Ding, Y. Qiu, K. Cai, Q. Yao, S. Chen, L. Chen, J. He, High performance n-type Ag 2 Se film on nylon membrane for flexible thermoelectric power generator, Nat. Commun., 10 (2019) 1-7.
[8] R. Niu, C. Pan, Z. Chen, L. Wang, L. Wang, Enhanced thermoelectric performance from self-assembled alkyl chain-linked naphthalenediimide/single walled carbon nanotubes composites, Chemical Engineering Journal, 381 (2020) 122650.
[9] C. Wan, X. Gu, F. Dang, T. Itoh, Y. Wang, H. Sasaki, M. Kondo, K. Koga, K. Yabuki, G.J. Snyder, Flexible n-type thermoelectric materials by organic intercalation of layered transition metal dichalcogenide TiS 2, Nature materials, 14 (2015) 622.
[10] T. Fang, X. Li, C. Hu, Q. Zhang, J. Yang, W. Zhang, X. Zhao, D.J. Singh, T. Zhu, Complex Band Structures and Lattice Dynamics of Bi<inf>2</inf>Te<inf>3</inf>-Based Compounds and Solid Solutions, Advanced Functional Materials, 29 (2019).
[11] Y. Sadia, Z. Aminov, D. Mogilyansky, Y.J.I. Gelbstein, Texture anisotropy of higher manganese silicide following arc-melting and hot-pressing, 68 (2016) 71-77.
[12] Y.J.J.o.e.m. Gelbstein, Pb 1− x Sn x Te alloys: Application considerations, 40 (2011) 533-536.
[13] G. Komisarchik, D. Fuks, Y.J.J.o.A.P. Gelbstein, High thermoelectric potential of n-type Pb1− x Ti x Te alloys, 120 (2016) 055104.
[14] G.M. Guttmann, D. Dadon, Y.J.J.o.A.P. Gelbstein, Electronic tuning of the transport properties of off-stoichiometric Pb x Sn1− x Te thermoelectric alloys by Bi2Te3 doping, 118 (2015) 065102.
[15] O. Appel, Y.J.J.o.e.m. Gelbstein, A comparison between the effects of Sb and Bi doping on the thermoelectric properties of the Ti 0.3 Zr 0.35 Hf 0.35 NiSn half-Heusler alloy, 43 (2014) 1976-1982.
[16] H. Song, Q. Meng, Y. Lu, K. Cai, Progress on PEDOT:PSS/Nanocrystal Thermoelectric Composites, Advanced Electronic Materials, DOI 10.1002/aelm.201800822(2019).
[17] K. Kanahashi, J. Pu, T. Takenobu, 2D Materials for Large-Area Flexible Thermoelectric Devices, Advanced Energy Materials, 10 (2020).
[18] X. Xiao, C.N. Kim, Y. Luo, X. Fan, Y. Deng, Performance Analysis of a Thermoelectric Generator with a Segmented Leg, J. Electron. Mater., 48 (2019) 7769-7779.
[19] S. Fan, Y. Gao, Numerical analysis on the segmented annular thermoelectric generator for waste heat recovery, Energy, 183 (2019) 35-47.
[20] E. Kanimba, M. Pearson, J. Sharp, D. Stokes, S. Priya, Z. Tian, A comprehensive model of a lead telluride thermoelectric generator, Energy, 142 (2018) 813-821.
[21] M. Picard, S. Turenne, D. Vasilevskiy, R.A. Masut, Numerical Simulation of Performance and Thermomechanical Behavior of Thermoelectric Modules with Segmented Bismuth-Telluride-Based Legs, Journal of Electronic Materials, 42 (2013) 2343-2349.
[22] S. Shittu, G. Li, X. Zhao, X. Ma, Y.G. Akhlaghi, E. Ayodele, Optimized high performance thermoelectric generator with combined segmented and asymmetrical legs under pulsed heat input power, Journal of Power Sources, 428 (2019) 53-66.
[23] Z.C. Liu, S.P. Zhu, Y. Ge, F. Shan, L.P. Zeng, W. Liu, Geometry optimization of two-stage thermoelectric generators using simplified conjugate-gradient method, Applied Energy, 190 (2017) 540-552.

[24] J.H. Meng, X.X. Zhang, X.D. Wang, Multi-objective and multi-parameter optimization of a thermoelectric generator module, Energy, 71 (2014) 367-376.
[25] J.W. Hearle, W.E. Morton, Physical properties of textile fibres, Elsevier2008.
[26] I.H. Kim, (Bi,Sb)2(Te,Se)3-based thin film thermoelectric generators, Materials Letters, 43 (2000) 221-224.
[27] M. Takashiri, T. Shirakawa, K. Miyazaki, H. Tsukamoto, Fabrication and characterization of bismuth-telluride-based alloy thin film thermoelectric generators by flash evaporation method, Sensors and Actuators, A: Physical, 138 (2007) 329-334.
[28] K. Suemori, S. Hoshino, T. Kamata, Flexible and lightweight thermoelectric generators composed of carbon nanotube-polystyrene composites printed on film substrate, Applied Physics Letters, 103 (2013).
[29] W. Zhu, Y. Deng, M. Gao, Y. Wang, Hierarchical Bi-Te based flexible thin-film solar thermoelectric generator with light sensing feature, Energy Conversion and Management, 106 (2015) 1192-1200.
[30] W. Lee, Y.H. Kang, J.Y. Lee, K.S. Jang, S.Y. Cho, Improving the thermoelectric power factor of CNT/PEDOT:PSS nanocomposite films by ethylene glycol treatment, Rsc Advances, 6 (2016) 53339-53344.
[31] L.M. Goncalves, P. Alpuim, G. Min, D.M. Rowe, C. Couto, J.H. Correia, Optimization of Bi2Te3 and Sb2Te3 thin films deposited by co-evaporation on polyimide for thermoelectric applications, Vacuum, 82 (2008) 1499-1502.
[32] J.A. Lee, A.E. Aliev, J.S. Bykova, M.J. de Andrade, D. Kim, H.J. Sim, X. Lepro, A.A. Zakhidov, J.B. Lee, G.M. Spinks, S. Roth, S.J. Kim, R.H. Baughman, Woven-Yarn Thermoelectric Textiles, Advanced Materials, 28 (2016) 5038-5044.
[33] K. Kato, Y. Hatasako, M. Uchino, Y. Nakata, Y. Suzuki, T. Hayakawa, C. Adachi, K. Miyazaki, Flexible Porous Bismuth Telluride Thin Films with Enhanced Figure of Merit using Micro-Phase Separation of Block Copolymer, Advanced Materials Interfaces, 1 (2014).
[34] S.Y. Huang, X.F. Xu, Parametric Optimization of Thermoelectric Generators for Waste Heat Recovery, Journal of Electronic Materials, 45 (2016) 5213-5222.
[35] L.H. Fan, G.B. Zhang, R.F. Wang, K. Jiao, A comprehensive and time-efficient model for determination of thermoelectric generator length and cross-section area, Energy Conversion and Management, 122 (2016) 85-94.
[36] G. Zhang, L. Fan, Z. Niu, K. Jiao, H. Diao, Q. Du, G. Shu, A comprehensive design method for segmented thermoelectric generator, Energy Conversion and Management, 106 (2015) 510-519.
[37] Z.Q. Niu, S.H. Yu, H. Diao, Q.S. Li, K. Jiao, Q. Du, H. Tian, G.Q. Shu, Elucidating modeling aspects of thermoelectric generator, International Journal of Heat and Mass Transfer, 85 (2015) 12-32.
[38] X. Hu, H. Takazawa, K. Nagase, M. Ohta, A. Yamamoto, Three-Dimensional Finite-Element Simulation for a Thermoelectric Generator Module, Journal of Electronic Materials, 44 (2015) 3637-3645.
[39] B. Jang, S. Han, J.Y. Kim, Optimal design for micro-thermoelectric generators using finite element analysis, Microelectronic Engineering, 88 (2011) 775-778.
[40] I.T. Witting, T.C. Chasapis, F. Ricci, M. Peters, N.A. Heinz, G. Hautier, G.J. Snyder, The Thermoelectric Properties of Bismuth Telluride, Advanced Electronic Materials, 5 (2019).
[41] G. Redlarski, A. Palkowski, M. Krawczuk, Body surface area formulae: an alarming ambiguity, Sci. Rep., 6 (2016) 27966.

[42] Z.L. Wang, Toward self-powered sensor networks, Nano Today, 5 (2010) 512-514.

Table 1 Parameters of material properties.

Material Property	α (μV K^{-1})	σ (S m^{-1})	κ (W m^{-1} K^{-1})
Polyimide (substrate)	0	0.5×10^{-17}	0.15
Silver wire	0	61.6×10^{6}	429
Bi_2Te_3 (n-type) [5]	-137.8	7.7×10^{3}	0.25
rGO [2]	19	1.45×10^{4}	3
Ag_2Se [7]	-140.7	4.97×10^{4}	0.50
NDI-10/90%SWCNT [8]	50.4	9.35×10^{4}	0.85
$TiS_2[(HA)_{0.08}(H_2O)_{0.22}(DMSO)_{0.03}$ [9]	-78	7.9×10^{4}	0.69

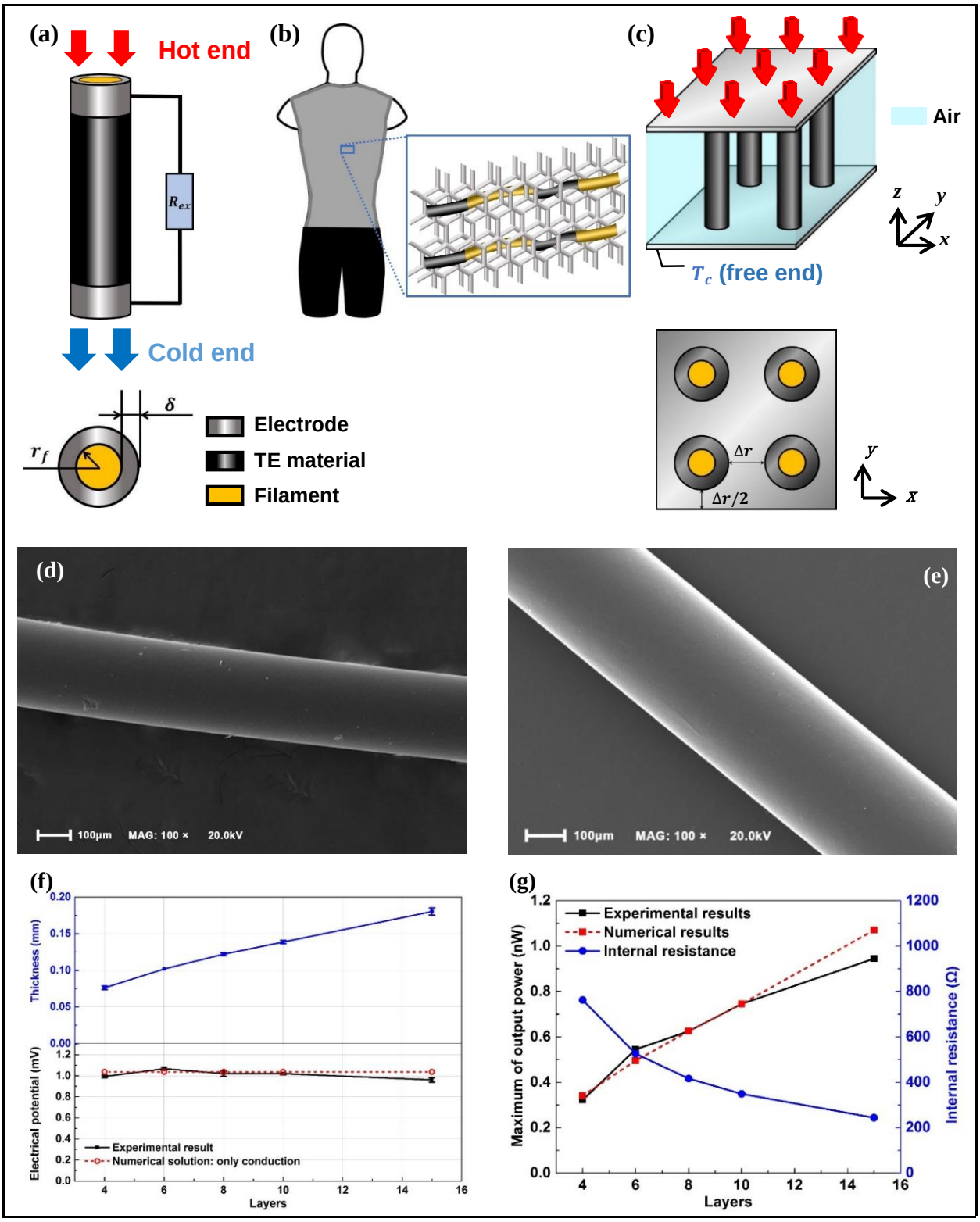

Fig. 1. (a) Schematic of a 1D FTEG unit connected with an external resistance. (b) Schematic of a FTEG device worn on the human torso back and an enlarged unit. (c) Schematic of a simplified unit cell of 1D FTEG array, and the cross-sectional configuration from top perspective. (d) SEM of original PET filament. (e) SEM of PEDOT: PSS coating on the PET filament. (f) Relationship between the thickness

of coating layers and electrical potential of fabricated FTEG. (g) Relationship between the thickness of coating layers, the internal resistance and maximum output of fabricated FTEG.

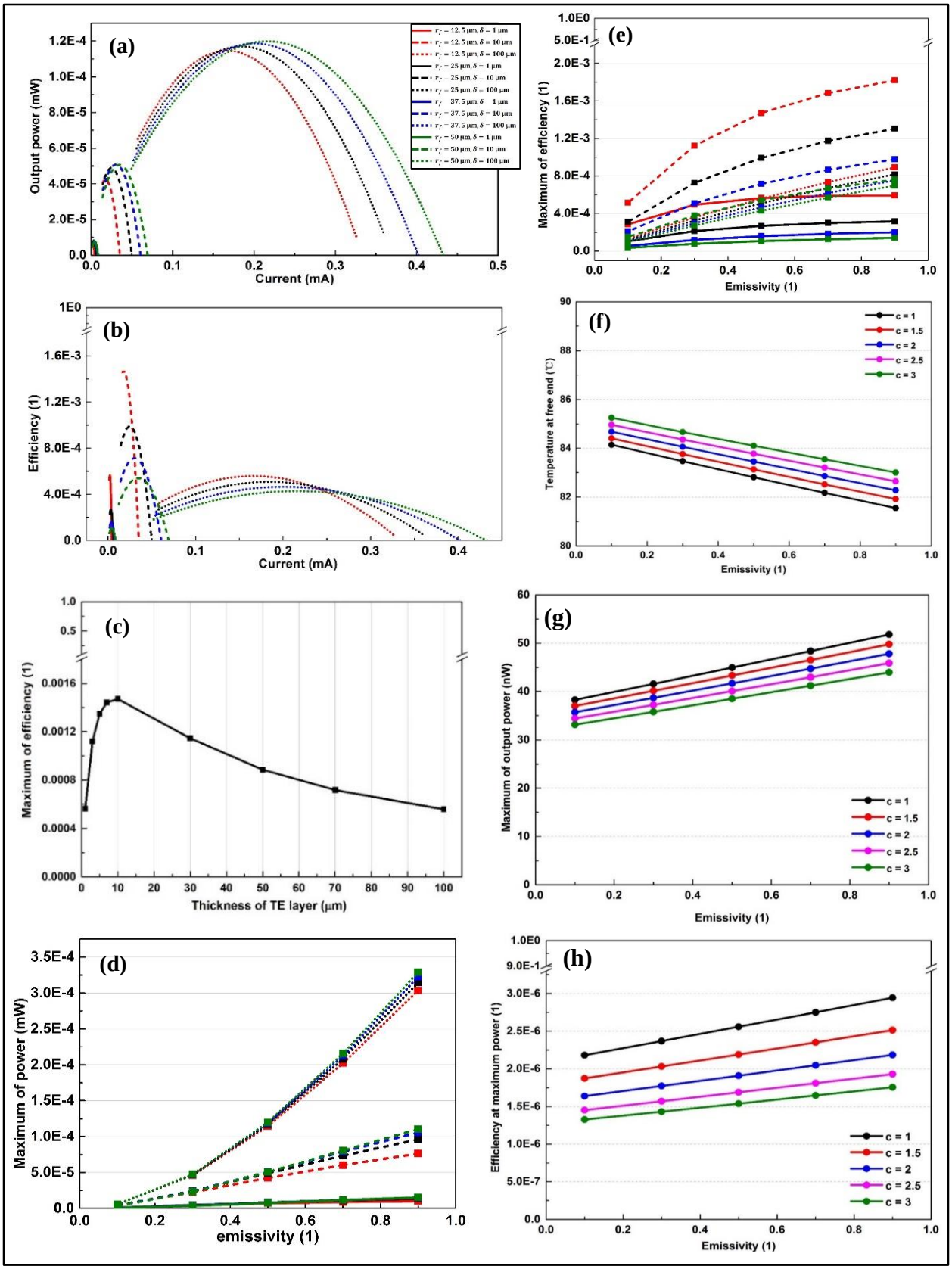
(a)
Output power (mW)
Current (mA)
(b)
Efficiency (1)
Current (mA)
(c)
Maximum of efficiency (1)
Thickness of TE layer (μm)
(d)
Maximum of power (mW)
emissivity (1)
(e)
Maximum of efficiency (1)
Emissivity (1)
(f)
Temperature at free end (℃)
Emissivity (1)
c = 1
c = 1.5
c = 2
c = 2.5
c = 3
(g)
Maximum of output power (nW)
Emissivity (1)
(h)
Efficiency at maximum power (1)
Emissivity (1)

Fig. 2. Effects of parameters on the performance of the fixed-free ends model: (a) and (b) the emissivity is 0.5; (c) the relationship between the TE thickness and the max efficiency. (d) and (e) the emissivity is changed. (f) The relationship between temperature at the free end and different emissivity for the 1D FTEG array, when the devices perform the maximum of output power. (g) The relationship between maximum of output power and different emissivity for the 1D FTEG array. (h) The relationship between efficiency at maximum power and different emissivity for the 1D FTEG array. (r_f is the radius of fiber; d is the thickness of TE layer; c is the controlled parameter.)

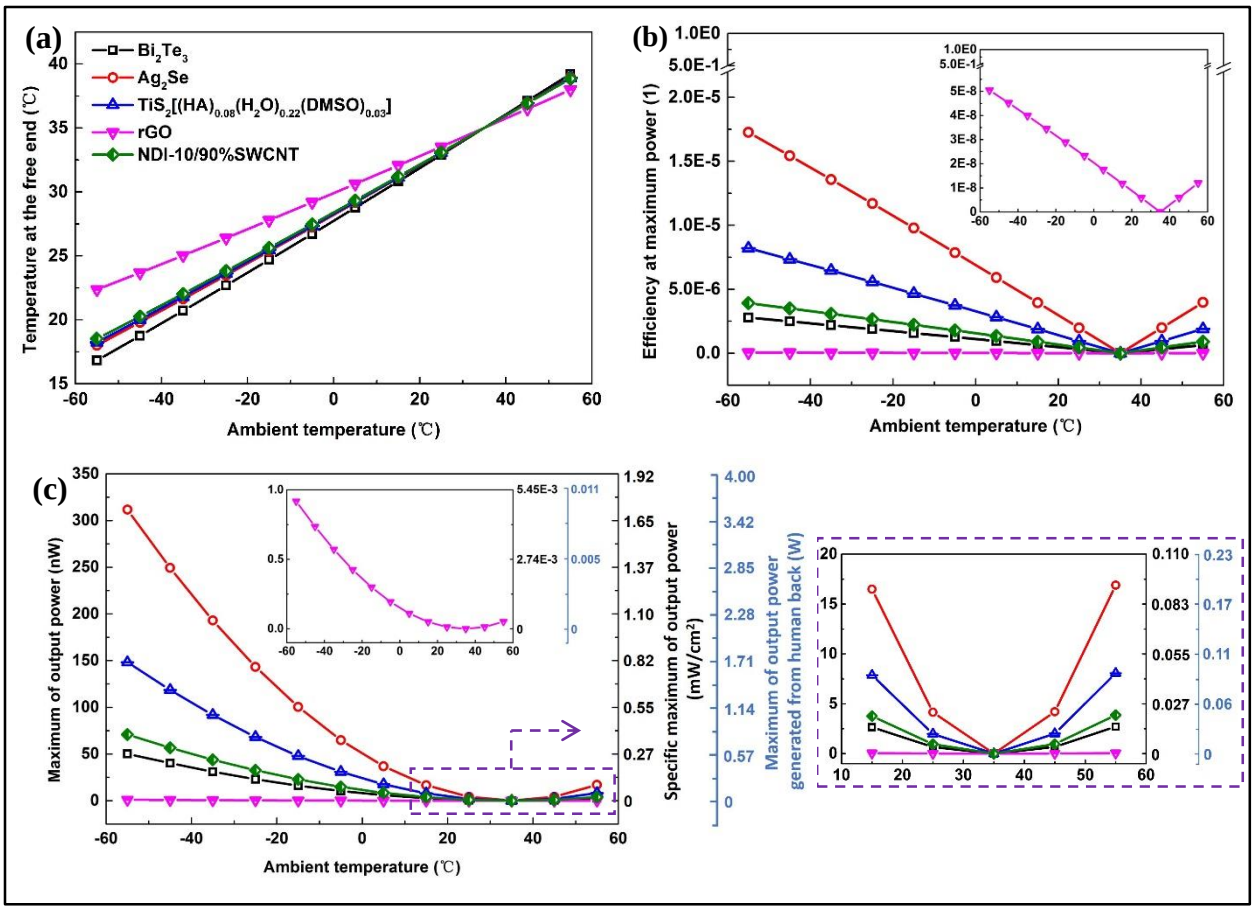

Fig. 3. Performance of array devices with different TE materials: (a) Relationship of the temperature at the free end and the ambient temperature. (b) Relationship of the maximum of output power of 1D FTEG array (the left longitudinal axis), the specific maximum of output power (the right inner longitudinal axis), the maximum of output power of the device with the area (0.208 m^2) equal to the human back (the right outer longitudinal axis), and the ambient temperature. (c) Relationship of the efficiency of maximum power and the ambient temperature.

Supplementary Information

Predicting Performance of Fiber Thermoelectric Generator Arrays in Wearable Electronic Applications

Li-sha Zhang [a], Bao Yang [a], Shu-pin Lin [a], Tao Hua [a], Xiao-ming Tao [a]*
[a] Research Center of Smart Wearable Technology, Institute of Textiles and Clothing, The Hong Kong Polytechnic University, Hong Kong, P.R. China
**xiao-ming.tao@polyu.edu.hk*

S1. Mathematical models

As shown in Fig. S1, a 1D FTEG suffers high temperature (T_h) at one end. But the cold end is free, at where the temperature is determined by the heat transfer: one situation is only conductive heat transfer; another is conductive and radiative heat transfer. The temperature distribution along the longitudinal direction will be deduced under these situations in the following part.

S1.1 Mathematical model of 1D FTEG with conductive heat transfer

Under only conductive heat transfer, no thermal energy releases through the radiation.

Assumptions:

(1) Steady-state conditions. (2) One-dimensional conduction in the *x*-direction. (3) Constant material properties. (4) No convections. (5) No radiations. (6) The fiber radius and thickness of TE layer are uniform along the longitudinal direction. (7) The boundary condition at the interface between the fiber surface and TE layer is same.

Boundary conditions:

1. $T(0) = T(x)_{x=0} = T_h$.
2. To approach to the free end, the difference of temperature distribution is regarded as zero: $\frac{dT}{dx} = 0$.

Analysis:

The 1D FTEG is composed of two parts: the fiber and the TE layer. Thus, their corresponding infinitesimally small control volume can be defined as: $dx \cdot \pi {r_f}^2$ and $dx \cdot \pi(\delta^2 + 2r_f\delta)$. The conduction heat rate through the fiber and the TE layer are $(q_f)_x$ and $(q_{TE})_x$, respectively, which are perpendicular to the controlled surfaces: $\pi {r_f}^2$ and $\pi(\delta^2 + 2r_f\delta)$.

For the fiber, the conduction heat rate through the controlled volume ($(q_f)_{x+dx}$) can be expressed as a Taylor series expansion (neglecting the higher-order terms):

$$(q_f)_x = -k_f(T) \cdot A_f \cdot \frac{dT}{dx} = -k_f(T) \cdot (\pi {r_f}^2) \cdot \frac{dT}{dx} \tag{S1}$$

Similarly, for the TE layer, conduction heat rate through the controlled volume ($(q_{TE})_{x+dx}$) can be expressed as a Taylor series expansion:

$$(q_f)_{x+dx} = (q_f)_x + \frac{d}{dx}\left((q_f)_x dx\right) \tag{S2}$$

$$(q_{TE})_x = -k_{TE}(T) \cdot A_{TE} \cdot \frac{dT}{dx} = -k_{TE}(T) \cdot \left[\pi\left(\delta^2 + 2r_f\delta\right)\right] \cdot \frac{dT}{dx} \tag{S3}$$

$$(q_{TE})_{x+dx} = (q_{TE})_x + \frac{d}{dx}\left((q_f)_x dx\right) \tag{S4}$$

In this system, Peltier effect and Joule heating attribute to the energy generation. The volumetric generation rate caused by Peltier effect is:

$$\dot{q}_{TE} = \frac{I \cdot \alpha(T) \cdot (T_x - T_{x+dx})}{\pi\left[\delta^2 + 2r_f\delta\right]dx} = J \cdot \alpha(T) \cdot \frac{dT}{dx} \tag{S5}$$

The volumetric generation rate caused by Joule heating is:

$$\dot{q}_{\Omega} = \frac{I^2 R_{TE}}{\pi\left(\delta^2 + 2r_f\delta\right)dx} = \frac{1}{\sigma_{TE}}(J)^2 \tag{S6}$$

Thus, the volumetric energy generation rate from the TE layer is:

$$\dot{q} = \dot{q}_{TE} - \dot{q}_{\Omega} = J \cdot \alpha \cdot \frac{dT}{dx} - \frac{1}{\sigma_{TE}}(J)^2 \tag{S7}$$

Besides, there is no energy generation in fiber, that is, $(\dot{E}_g)_f = 0$. Thus, the energy generation rate in this system is:

$$\dot{E}_g = (\dot{E}_g)_{TE} = \dot{q} \cdot (dx) \cdot \pi(\delta^2 + 2r_f\delta) \tag{S8}$$

The system follows the energy balance:

$$\dot{E}_{in} - \dot{E}_{out} + \dot{E}_g = 0 \tag{S9}$$

$$\left[(q_f)_x + (q_{TE})_x\right] - \left[(q_f)_{x+dx} + (q_{TE})_{x+dx}\right] + \dot{q} \cdot (dx) \cdot \pi(\delta^2 + 2r_f\delta) = 0$$

$$\left(\frac{{r_f}^2 k_f}{\delta^2 + 2r_f\delta} + k_{TE}\right) \cdot \frac{d^2T}{dx^2} + J \cdot \alpha \cdot \frac{dT}{dx} - \frac{1}{\sigma_{TE}}(J)^2 = 0 \tag{S10}$$

The thermal conductivity of fiber and TE layer are constants. The geometry of fiber and TE layer does not change. Eqn.(10) is as follow:

$$\frac{d^2T}{dx^2} + J \cdot \frac{\alpha}{k} \cdot \frac{dT}{dx} - \frac{J^2}{\sigma_{TE} k} = 0 \tag{S11}$$

where the effective thermal conductivity is $k = \frac{{r_f}^2 k_f}{\delta^2 + 2 r_f \delta} + k_{TE}$.

Under stationary conditions, the current density J is a constant. Thus, let $a = J \cdot \frac{\alpha}{k}$, $b = \frac{J^2}{\sigma_{TE} k}$. To substitute them into the above equation, we can get:

$$\frac{d^2T}{dx^2} + a\frac{dT}{dx} - b = 0 \tag{S12}$$

$$\frac{dT}{dx} + aT(x) = bx + C_0$$

where C_0 is a constant. To multiply the integration factor e^{ax} to the both sides of the above equation:

$$e^{ax} \cdot \frac{dT}{dx} + ae^{ax}T(x) = (bx + C_1)e^{ax}$$

$$\int \frac{d[T(x)e^{ax}]}{dx} = \int (bx + C_1)e^{ax}\, dx + C_2$$

where C_2 is a constant.

$$T(x) = \frac{b}{a^2}(ax - 1) + C_2 e^{-ax} + \frac{C_1}{a} \tag{S13}$$

According to the boundary condition #1:

$$T(0) = -\frac{b}{a^2} + C_2 + \frac{C_1}{a} = \mathrm{T_h}$$

According to the boundary condition #2, $a = J \cdot \frac{\alpha}{k} > 0$:

$$\left.\frac{dT}{dx}\right]_{x\to\infty} = (\frac{b}{a} - C_2 a e^{-ax})_{x\to\infty} = 0$$

Thus,

$$C_2 = \frac{b}{a^2}$$

$$C_1 = aT_h$$

To substitute into Eqn.(12):

$$T(x) = \frac{k}{\sigma_{TE}\alpha^2}\left(J \cdot \frac{\alpha}{k} \cdot x + e^{-J\cdot\frac{\alpha}{k}x} - 1\right) + T_h \quad \text{(S14)}$$

Note that $k = \frac{{r_f}^2 k_f}{\delta^2 + 2r_f\delta} + k_{TE}$.

S1.2 Mathematical model of 1D FTEG with conductive and radiative heat transfer

Under conductive and radiative heat transfer, some thermal energy is transmitted through the conduction from the hot to cold ends; meanwhile, some is released from the surface in the radiation form. Thus, the assumptions are same to the former section, except for (5). The surface of 1D FTEG is opaque, diffuse and grey. The boundary conditions are same to the former part.

Analysis:

The surface of the infinitesimally small control volume is

$$dA_s = 2\pi(r_f + \delta) \cdot dx \tag{S15}$$

The radiation releasing from this surface can be given by:

$$dq_{rad} = \sigma_{SB}\varepsilon(T_s^4 - T_{sur}^4) \cdot \ dA_s = \sigma_{SB}\varepsilon(T_s^4 - T_{sur}^4) \cdot 2\pi(r_f + \delta) \cdot dx \tag{S16}$$

According to Eqn. (S9), the system follows the energy balance:

$$\left[\left(q_f\right)_x + (q_{TE})_x\right] - \left[\left(q_f\right)_{x+dx} + (q_{TE})_{x+dx}\right] - dq_{rad} + \dot{q} \cdot (dx) \cdot \pi(\delta^2 + 2r_f\delta) = 0$$

$$\left(\frac{{r_f}^2 k_f}{\delta^2 + 2r_f\delta} + k_{TE}\right) \cdot \frac{d^2T}{dx^2} - \frac{2(r_f + \delta)}{\delta^2 + 2r_f\delta} \cdot \sigma_{SB}\varepsilon(T_s^4 - T_{sur}^4) + \ J \cdot \alpha \cdot \frac{dT}{dx} - \frac{J^2}{\sigma_{TE}} = 0 \tag{S17}$$

Under steady state, the surface temperature of 1D FTEG is equal to the temperature of TE layer, $T = T_s$. If the surrounding temperature is a constant, Eqn. (17) can be written as:

$$\frac{d^2T}{dx^2} + C_1\frac{dT}{dx} = C_2T^4 + C_3 \tag{S18}$$

$$C_1 = \frac{\left(\delta^2 + 2r_f\delta\right) \cdot \ J \cdot \alpha}{{r_f}^2 k_f + \left(\delta^2 + 2r_f\delta\right)k_{TE}}$$

$$C_2 = \frac{2(r_f + \delta) \cdot \sigma_{SB}\varepsilon}{{r_f}^2 k_f + \left(\delta^2 + 2r_f\delta\right)k_{TE}}$$

$$C_3 = \left(\frac{J^2}{\sigma_{TE}} - \frac{2(r_f + \delta)}{\delta^2 + 2r_f\delta} \cdot \sigma_{SB}\varepsilon \cdot T_{sur}^4\right) \cdot \frac{\delta^2 + 2r_f\delta}{{r_f}^2 k_f + \left(\delta^2 + 2r_f\delta\right)k_{TE}}$$

To multiply $e^{C_1 x}$ at the two sides of Eqn. (S18) and to integrate:

$$\int e^{C_1 x}\left(\frac{d^2T}{dx^2} + C_1\frac{dT}{dx}\right)dx = \int e^{C_1 x}(C_2T^4 + C_3)\,dx + C_0 \qquad (C_0 \text{ is a constant})$$

$$e^{C_1 x}\frac{dT}{dx} = C_2\int e^{C_1 x}T^4\,dx + \frac{C_3}{C_1}\cdot e^{C_1 x} + C_0 \tag{S19}$$

Let $T = T(x) = Ae^{\lambda x}$ ($\lambda \neq 0$). Then, $\frac{dT}{dx} = A\lambda e^{\lambda x} = \lambda T$. Thus, Eqn. (S19) can be written as:

$$e^{C_1 x}\cdot\lambda T = \frac{C_2A^4}{C_1 + 4\lambda}\int e^{(C_1+4\lambda)x}\,d[(C_1 + 4\lambda)x] + \frac{C_3}{C_1}\cdot e^{C_1 x} + C_0$$

$$T - \frac{C_2}{(C_1 + 4\lambda)\cdot\lambda}T^4 = \frac{C_3}{C_1\cdot\lambda} + \frac{C_0}{\lambda}e^{-C_1 x} \tag{S20}$$

Thus, the temperature distribution of 1D FTEG along the conductive heat transfer can only be expressed in an implicit solution.

S2. Influence of contact resistance

Thermal and electrical contact resistance (TCR and ECR) diminishes the output power and efficiency of devices. Although this result has been discussed in the reference [1], the temperature distribution under contact resistance condition has not been illustrated. Therefore, if the hot and cold sides temperature is 100 ℃ and 25 ℃, respectively, the influence of TCR and ECR on the temperature distribution along 1D FTEG and the device performance is illustrated in Fig. S2. In order to study the influence of TCR, the thermal contact conductivity was set as 2×10^3 W/m^2 ·

K for the 1D FTEG whose fiber radius and thickness of TE layer were 50 μm and 10 μm, respectively. In Fig. S2(a), the curves are almost overlapped, whose slopes are dependent on the thermal conductivity of materials. But by enlarging Fig. S2(a) round the two interfaces position, Fig. S2(b) and (c) shows the departure of the red and black lines, because of the TCR. The temperature at the hot side of the TE material in the model with TCR is lower than that without TCR, it at the cold side with TCR is higher than that without TCR. Thus, the temperature difference between the hot and cold sides with TCR is lower than that without TCR. TCR directly attenuates the output power and efficiency, as shown in Fig. S2(d). For studying the influence of ECR, the electrical contact conductivity was set as $1\times 10^{7}\ \mathrm{S/m^{2}}$. In Fig. S2(e), the temperature distribution along 1D FTEGs with and without ECR is exactly overlapped, because ECR is immaterial on the thermal resistance. ECR can be treated as an external resistance, when the FTEG is in a circuit. Thus, as shown in Fig. S2(f), the output power and efficiency are reduced, due to the existence of ECR.

S3. Analytical and numerical solutions of traditional TEGs

To select the appropriate structure, the performance of TEGs, which are designed in different structures: π-structure, S-structure and Ⅱ-structure, is calculated and compared in this section. In order to totally focus on the influence of the different structures on the performance of TEGs, the material parameters are designated and listed in Table S1. All the TE legs in each case is designed as a cubic whose edge is 1cm. The distance between two legs is 1 cm. For each case, the geometric parameters of electrodes are listed in Table S2. The assumptions are as follow: (1) only conductive heat transfer takes place, without radiative and connective heat transfer; (2) the contact resistance can be ignored. Besides, the boundary condition is that the temperature at the hot and cold side is

fixed as 400 K and 300 K, respectively. Fig. S3 shows the schematic of TEGs in different structures and its corresponding equivalent electrical and thermal resistance circuit. The analytical solution of traditional TEGs in different structures is thoroughly investigated (Table S3).

The thermal resistance (θ) of material is determined by the thermal conductivity (κ), the cross-sectional area (A) that is perpendicular to the heat flow, and the length (L) along which the heat flow passes, which can be given by

$$\theta = \frac{L}{\kappa \cdot A}$$

The resistance of the N- and P- type TE leg is calculated as the following:

$$R_P = R_N = \frac{1}{\sigma_N} \cdot \frac{L}{A_N}$$

At the max power, the efficiency of the TEG is given by:

$$\eta_{max} = \frac{P_{max}}{q_{in}}$$

Based on the material properties and geometric parameters in Table S1 and S2, the calculation results of these models have been illustrated in Table S4. If the TE legs are composed of p- and n-type TE materials, the generator should be fabricated in π-structure. If the TE legs are composed of only one type TE materials, the device should be fabricated in Ⅱ-structure.

S4. Simulation results of single 1D FTEG under only conductive heat transfer

In Fig. S3, if the cross-sectional area of TE layer is same, the maximum of power linearly decreases with the increase of length. While the length is same, the power increases with the increment of the cross-sectional area that is determined by the thickness of TE layer and the fiber radius. Based on Eqn. (1), when the temperature difference and material are invariable, the electrical potential caused by the Seebeck effect is a constant. Compared with the fiber radius, the thickness of TE layer changed in orders of magnitude is the primary factor in the difference of power. This phenomenon can be explained with Eqn. (3) ~ (5). Therefore, under only conductive heat transfer, the power can be optimized with shortening the length of TE layer or enlarging the cross-sectional area of TE layer by increasing the thickness of TE layer and the fiber radius. If the input heat rate is same, the increase of the maximum of power leads to the increment of efficiency.

S5. Materials and their properties

S5.1. Materials

The PEDOT: PSS was 5.0wt% conductive screen printable ink, which was labelled as Orgacon^{TM} EL-P-5015. It was used directly without any purification. PET monofilament was specified that its diameter and fineness was 0.25 mm 600 denier (D), respectively. It was obtained from Nantong Ntec Monofilament Technology Company.

S5.2. Thermoelectric properties of PEDOT: PSS

In order to measure Seebeck coefficient, thermal conductivity and electrical conductivity, PEDOT: PSS was dried in an oven at 90 ℃ for 24 hours before grinding into extremely fine powder. The powder was pressed into two pellets for the measurement of TE properties. The

diameter was about 13 mm, and the thickness was approximate 1.10 mm and 1.27 mm. SBA 458 Nemesis measurement Setup (NETZSCH Group, German) was applied to obtain the Seebeck coefficient and electrical conductivity in the in-plane direction. The thermal conductivity was obtained from a laser flash apparatus (LFA 457 MicroFlash, NETZSCH Group, German). The process was conducted in argon gas at atmospheric pressure. The temperature range during the measurement process was from 296 K to 420 K. For measuring thermal conductivity, the temperature was raised up with $1\ \mathrm{K}\cdot\mathrm{min}^{-1}$ before reaching 343 K and then with $3\ \mathrm{K}\cdot\mathrm{min}^{-1}$ until arriving at 420 K.

Fig. S5 shows the thermoelectric properties of PEDOT: PSS. Those properties were initially measured at 296 K, which were recorded again at 320 K. Then, they were measured when the temperature increased every 20 K until to 420 K. Firstly, the line of Seebeck coefficient begins at $15.03\ \mu\mathrm{V}\cdot\mathrm{K}^{-1}$ and increases to the maximum of $16.83\ \mu\mathrm{V}\cdot\mathrm{K}^{-1}$ at 420 K. Secondly, the initial value of electrical conductivity is $641\ \mathrm{S}\cdot\mathrm{m}^{-1}$ and the peak is $759\ \mathrm{S}\cdot\mathrm{m}^{-1}$ at 400 K. The tendency of the electrical conductivity of PEDOT: PSS is similar to the published article [2]. Besides, the range of Seebeck coefficient and electrical conductivity is same to the reported work [3].

S5.3. TGA of PEDOT: PSS

The PEDOT: PSS ink was firstly dried in a vacuum oven at 90 ℃ for 24 hrs, in order to evaporate part of solvent. Otherwise, the existence of too much solvent would cause inaccuracy in the following measurement[4]. Then, thermo-gravimetric analysis (TGA) for the dried PEDOT: PSS was completed in nitrogen condition through TGA/DSC 1 STAR^{e} System that includes data collection and analysis supporting software. The temperature was rose up from 50 ℃ to 700 ℃ at rate of $10℃/\mathrm{min}$. The result of TGA measurement would provide the proper temperature range

for the following fabrication process, as shown in **Fig. S6**. Because the sample has been dried at 90 ℃ before the measurement, the beginning parts of the curve shows little weight loss when the temperature is lower than about 75 ℃. A slight drop of the line occurs around 100℃, which may be caused by the evaporation of moisture caught by the PSS[4]. Before the temperature increasing to 350 ℃, the rate of weight percentage becomes gradually rapid, as the tangent slope of the curve increments. This follows by suddenly falling down at approximately 350 ℃. Such behavior of PEDOT: PSS has also been observed in some published articles[4, 5]. When the temperature is above 500 ℃, the residual weigh tends to stay at ~30%. Thus, this PEDOT: PSS ink should be appropriately applied within 100℃ to prevent its decomposition from the effect of high temperature.

S5.4. Measurement system of electrical potential of 1D FTEGs

The electrical potential of these 1D FTEGs is measured with the lab-made measurement system. This system was composed of three parts: a heat source, a real-time temperature measurement apparatus and an output electrical potential measurement apparatus. Whtalent® TEC Temperature Control system, the heat source, generated and maintained the high and low temperature at 105 ℃ and 20 ℃, respectively. The real-time temperature of hot and cold plates was 88 ± 1 ℃ and 22 ± 1 ℃, respectively, which was measured by anbai® Applent AT4516 16-Channel Temperature Meter with probes fixed on the surface of plates. And the electrical potential was displayed with Model 2700 Multimeter/Switch System, a Keithley instrument.

S6 Comparison of the performance of single 1D FTEG and its array

Fig. S9 shows the temperature distribution of the TE layer along the longitudinal direction of 1D FTEG single and array models. In **Fig. S9(a),** the slope of the red straight line is determined by the thermal conductivity of the TE material, because the heat energy is only transported by the conduction. But, when the radiation is considered, the black curve is below the red one. That is, under the conduction and radiation, some heat energy is transmitted through the radiative heat transfer, except for the conductive heat transfer. Thus, the temperature along the longitudinal direction is lower than the case under only conduction. This results in the higher maximum of output power under the conduction and radiation condition. Similarly, in **Fig. S9(b),** the red curve is above the black one. But they are in S-shape, which are quite different from their counterparts in **Fig. S9(a).** The conductive heat transfer through the air happens in the 1D FTEG array models, which affects the temperature distribution along the longitudinal direction. Compared with **Fig. S9(a),** in Fig. **S9(b),** the temperature difference between the hot and cold ends is smaller; the difference between the red and black curves is less. Thus, the maximum of output power and efficiency in the 1D FTEG array is same, under different conditions.

Table S6 shows the temperature at cold end, maximum of power and maximum of efficiency of 1D FTEG single and array models, under two different condition: the conduction and radiation, or only the conduction. In the simulation, the cold end temperature under the conduction and radiation was obtained from the models, which was a free end. Then, this temperature was set as the constant in the models under only conductive heat transfer. Meanwhile, the hot end temperature and the emissivity in all cases was 100 ℃ and 0.5, respectively. For the 1D FTEG single model, when the temperature at the cold end is same, the maximum of output power should be same.

However, in **Table S6**, it is larger under the conduction and radiation than that under the only conduction. This is the result of the different temperature distribution along the longitudinal direction (**Fig. S9(a)**). But for the 1D FTEG array model, although the temperature distribution is not overlapped (**Fig. S9(b)**), the maximum of output power is same under both conditions. The reason is the temperature difference between the hot and cold ends is only 15.5 ℃, which is not larger enough to cause the significant influence on the power. Besides, for the 1D FTEG single model, when the output power is the maximum, the efficiency under the conduction and radiation is smaller than that under the only conduction, because some energy is wasted through the radiation into the surroundings where the temperature is 25 ℃. However, for the 1D FTEG array model, the efficiency is same under different condition. The explanation is that the primary approach to transfer the heat energy is the conductive heat transfer through the filament, TE layer, and air (Fig. 1(d)). Although the radiation causes the temperature at the cold end is lower than that at the hot end, a little of energy is transmitted by this method, according to Eqn. (2). Compared the single and array model, the efficiency shows the difference in three orders of magnitude. This is the result that much energy is transported from the hot to cold ends by the conductive heat transfer through the air in the array model.

S7 Calculation of FTEG device worn on human back

Suppose the FTEG device is composed of 1D FTEG arrays, which is worn on the back of a human torso. According to the results in the Section 3.2, when the control parameter, c, was equal to 1, the power and efficiency of 1D FTEG array was higher than other situations. Thus, in this simulation, $c = 1$. The emissivity is set as a constant, $\varepsilon = 0.5$. And the external resistance is shown in Table S7, which was equal to the internal resistance. The filament radius: $r_f = 12.5\ \mu$m.

The thickness of TE layer: $d = 10\ \mu$m. Thus, the length of the side of square (as shown in Fig. 1(d)) can be calculated:

$$l = 2 \cdot \left(\frac{\Delta r}{2}\right) + 2 \cdot 2\left(\mathrm{d} + r_f\right) + \Delta r = 1.35 \times 10^{-2}\ \mathrm{cm}$$

Thus, the cross-sectional area can be calculated:

$$A_c = l^2 = 1.82 \times 10^{-4}\ \mathrm{cm}^2$$

The specific maximum of power can be given by:

$$(P_{max})_s = \frac{P_{max}}{A_c}$$

The maximum of power generated by the human back can be given by:

$$(P_{max})_{hb} = (P_{max})_s \times A_{hb}$$

where A_{hb} is the area of the human back, $0.208\ \mathrm{m}^2$.

References

[1] Z.L. Ouyang, D.W. Li, Modelling of segmented high-performance thermoelectric generators with effects of thermal radiation, electrical and thermal contact resistances, Scientific Reports, 6 (2016).
[2] Y. Kim, A.M. Ballantyne, J. Nelson, D.D.C. Bradley, Effects of thickness and thermal annealing of the PEDOT:PSS layer on the performance of polymer solar cells, Organic Electronics, 10 (2009) 205-209.
[3] S. Hata, T. Omura, K. Oshima, Y. Du, Y. Shiraishi, N. Toshima, Novel Preparation of Poly (3, 4-ethylene dioxythiophene)-Poly (styrenesulfonate)-Protected Noble Metal Nanoparticles as Organic-Inorganic Hybrid Thermoelectric Materials, Bull. Soc. Photogr. Imag. Japan, 27 (2017) 13-18.
[4] K. Xu, G. Chen, D. Qiu, Convenient construction of poly(3,4-ethylenedioxythiophene)-graphene pie-like structure with enhanced thermoelectric performance, Journal of Materials Chemistry A, 1 (2013) 12395-12399.

[5] M. Culebras, C.M. Gómez, A. Cantarero, Thermoelectric measurements of PEDOT:PSS/expanded graphite composites, Journal of Materials Science, 48 (2013) 2855-2860.

Table S1. The properties of TE materials and electrode in the model for studying the influence of different structures.

	N-type TE material	**P-type TE material**	**Silver**
Seebeck coefficient (μV/K)	-195	195	--
Electrical conductivity (S/m)	7.41×10^4	7.41×10^4	6.16×10^7
Thermal conductivity (W/m·K)	1.4	1.4	429

Table S2. Geometric parameters of electrode for the traditional TEGs in different structures.

Electrode geometry	**π-structure**		**S-structure**		**Ⅱ-structure**		
	up	**down**	**up**	**down**	**up**	**down**	**perpendicular**
Width (cm)	3	1	3	1	1.5 (right) 1 (left)	1 (right) 1.6 (left)	0.1
Depth (cm)	1						1
Height (cm)	0.1						1

Table S3 Equations of the properties and performance of TEGs in different structures.

	π-structure	**S-structure**	**Ⅱ-structure**
Thermal conductance, K	$\frac{1}{\theta_N + 2\theta_e} + \frac{1}{\theta_P + 2\theta_e}$	$\frac{1}{\theta_N + 2\theta_e} + \frac{1}{\theta_{em}} + \frac{1}{\theta_N + 2\theta_e}$	$\frac{1}{\theta_N + 2\theta_e} + \frac{1}{\theta_N + 2\theta_e}$
Electrical potential, ΔU	$(\alpha_P - \alpha_N)\Delta T$	$2\alpha_N \Delta T$	$\alpha_N \Delta T$
The maximum of power, P_{max}	$\frac{(\Delta U)^2}{4(R_N + R_P)}$	$\frac{(\Delta U)^2}{4(2R_N)}$	$\frac{(\Delta U)^2}{4(R_N/2)}$
Current at the maximum power, I	$\frac{\Delta U}{2(R_N + R_P)}$	$\frac{\Delta U}{2R_N + R_{ex}}$	$\frac{\Delta U}{\frac{R_N}{2} + R_{ex}}$
Heat rate flowing into the TEG, q_{in}	$(\alpha_P - \alpha_N) \cdot T_h \cdot I + K(T_h - T_c) - \frac{1}{2} I^2 R_{ex}$	$(2\alpha_N) \cdot T_h \cdot I + K(T_h - T_c) - \frac{1}{2} I^2 R_{ex}$	$\alpha_N \cdot T_h \cdot I + K(T_h - T_c) - \frac{1}{2} I^2 R_{ex}$

Table S4 Calculation results of the performance of TEG in different structures.

	π-structure	**S-structure**	**Ⅱ-structure**
Thermal conductance (W/K)	2.80×10^{-2}	38.5×10^{-2}	2.80×10^{-2}
Electrical potential (V)	39×10^{-3}	39×10^{-3}	19.5×10^{-3}
The maximum of power (mW)	140.8	140.8	140.8
Current at the maximum power (A)	7.22	7.22	14.4
Heat rate flowing into the TEG (W)	3.86	39.55	3.83
Efficiency at the maximum power	0.0365	0.0036	0.0367

Table S5. Thickness and performance of 1D FTEG samples

Layers	**4**	**6**	**8**	**10**	**15**
Thickness (mm)	0.07625 ±0.00236	0.10190 ±0.00000	0.12212 ±0.00188	0.13867 ±0.00243	0.18027 ±0.00428
Electrical potential (mV)	0.99±0.01	1.07±0.02	1.02±0.03	1.02±0.01	0.96±0.02
Internal resistance (Ω)	762	526	416	349	244
Experimental maximum output power (nW)	0.322	0.545	0.625	0.745	0.945
Numerical maximum output power (nW)	0.341	0.495	0.625	0.745	1.070

Table S6. Temperature at cold end (T_c), the maximum of power (P_{max}) and the maximum of efficiency (η_{max}) of 1D FTEG single and array models under different condition: conduction and radiation, or only conduction.

	1D FTEG single model		**1D FTEG array model**	
	Conduction and radiation	**Only conduction**	**Conduction and radiation**	**Only conduction**
$\boldsymbol{T_c}$ **(℃)**	66.6		84.5	
$\boldsymbol{P_{max}}$ **(nW)**	42.3	41.1	36.6	36.6
$\boldsymbol{\eta_{max}}$ **(1)**	1.47×10^{-3}	3.45×10^{-3}	2.03×10^{-6}	2.03×10^{-6}

Table S7. External resistance connected with the 1D FTEG array of different TE materials

	Bi_2Te_3	rGO	Ag_2Se	NDI-10/90%SWCNT	$TiS_2[(HA)_{0.08}(H_2O)_{0.22}(DMSO)_{0.03}$
External resistance (Ω)	29.6	15.7	4.6	2.5	2.9

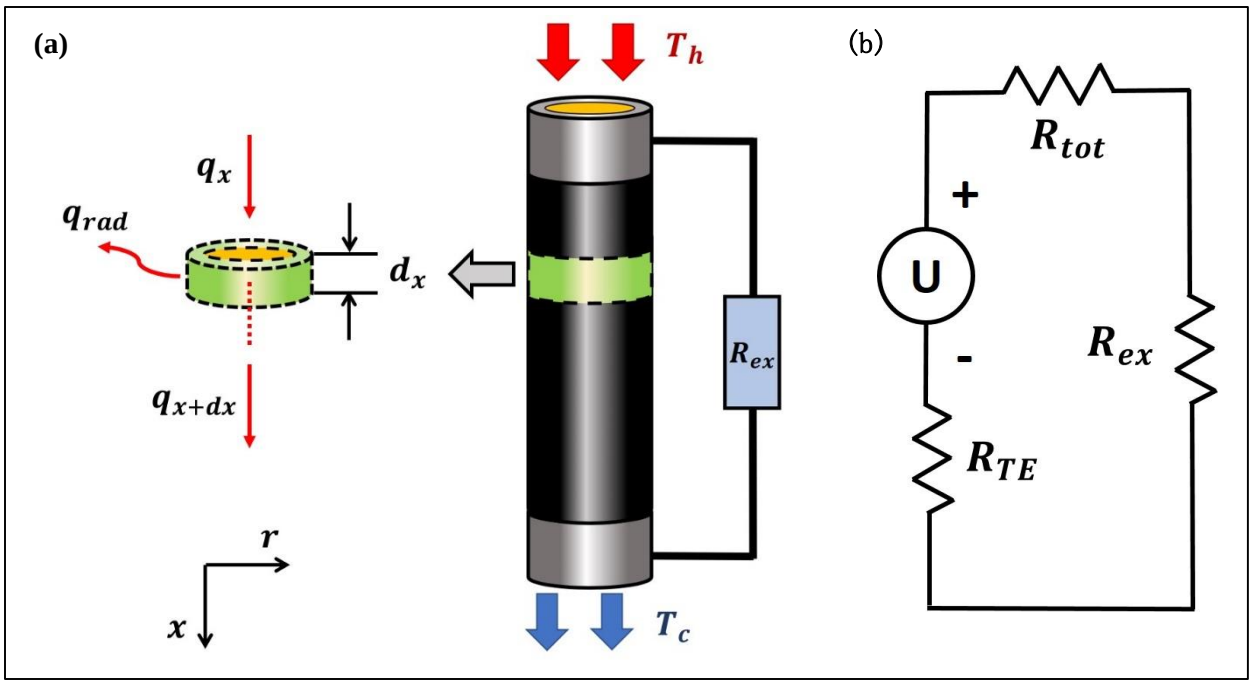

Fig. S4 (a) Schematic of heat transfer in a single 1D FTEG. (b) Equivalent electric circuits.

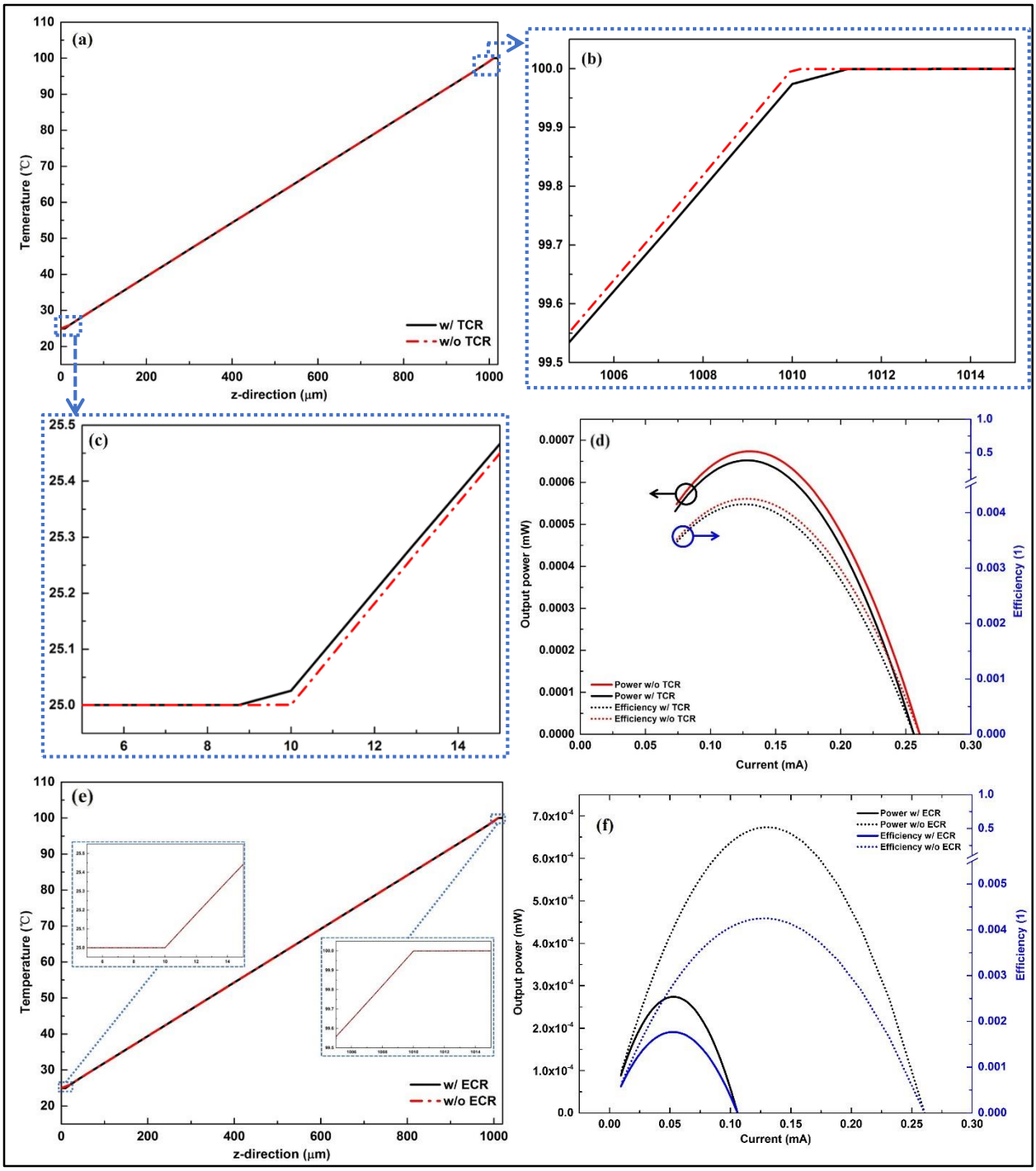

Fig. S2 The influence of TCR on: **(a) ~ (c)** the temperature distribution along 1D FTEG; **(d)** the output power and efficiency. The influence of ECR on: **(e)** the temperature distribution along 1D FTEG; **(f)** the output power and efficiency.

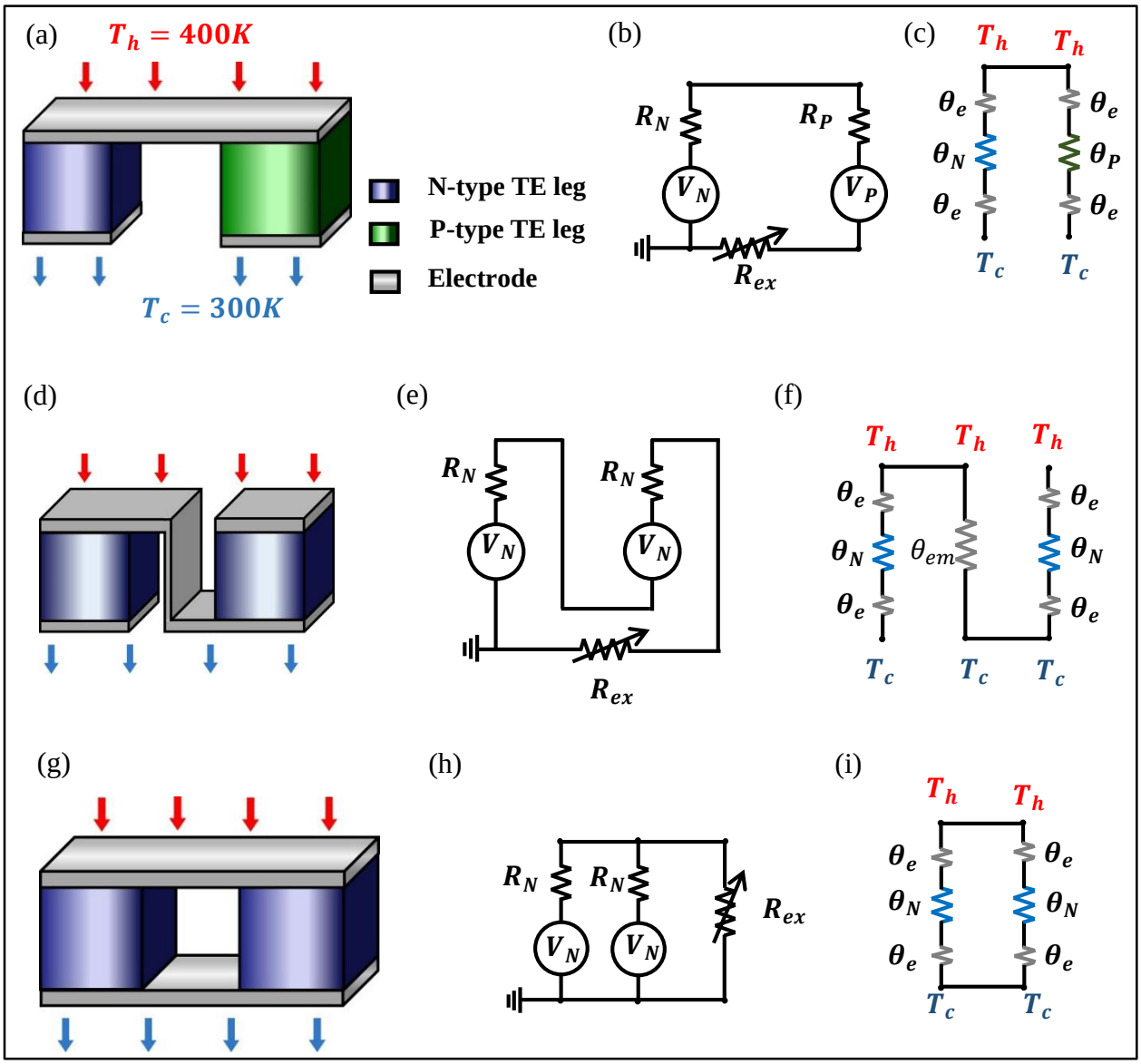

Fig. S3 Schematic, the equivalent circuit of TEG with external resistance and the thermal resistance circuit: (a), (b) and (c) TEG in π-structure; (d), (e) and (f) TEG in S-structure; (g), (h) and (i) TEG in || -structure.

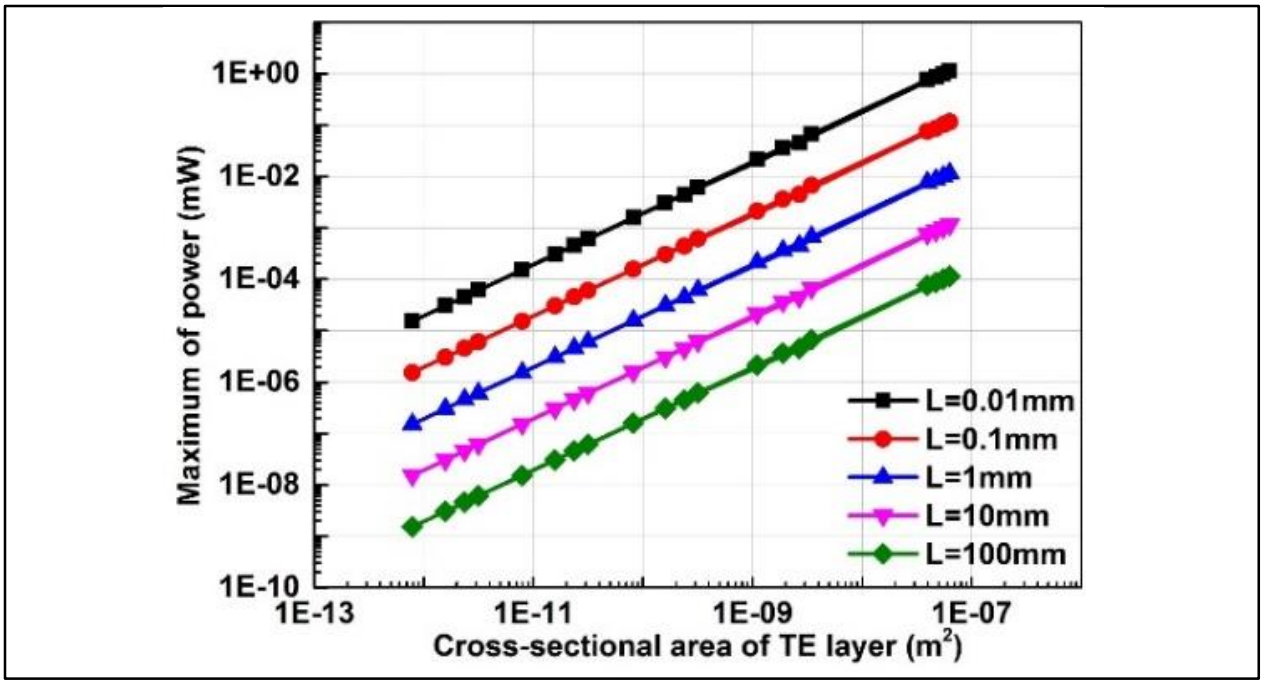

Fig. S4 The maximum of power of 1D FTEG under only conduction situation. (L is the length of the TE layer)

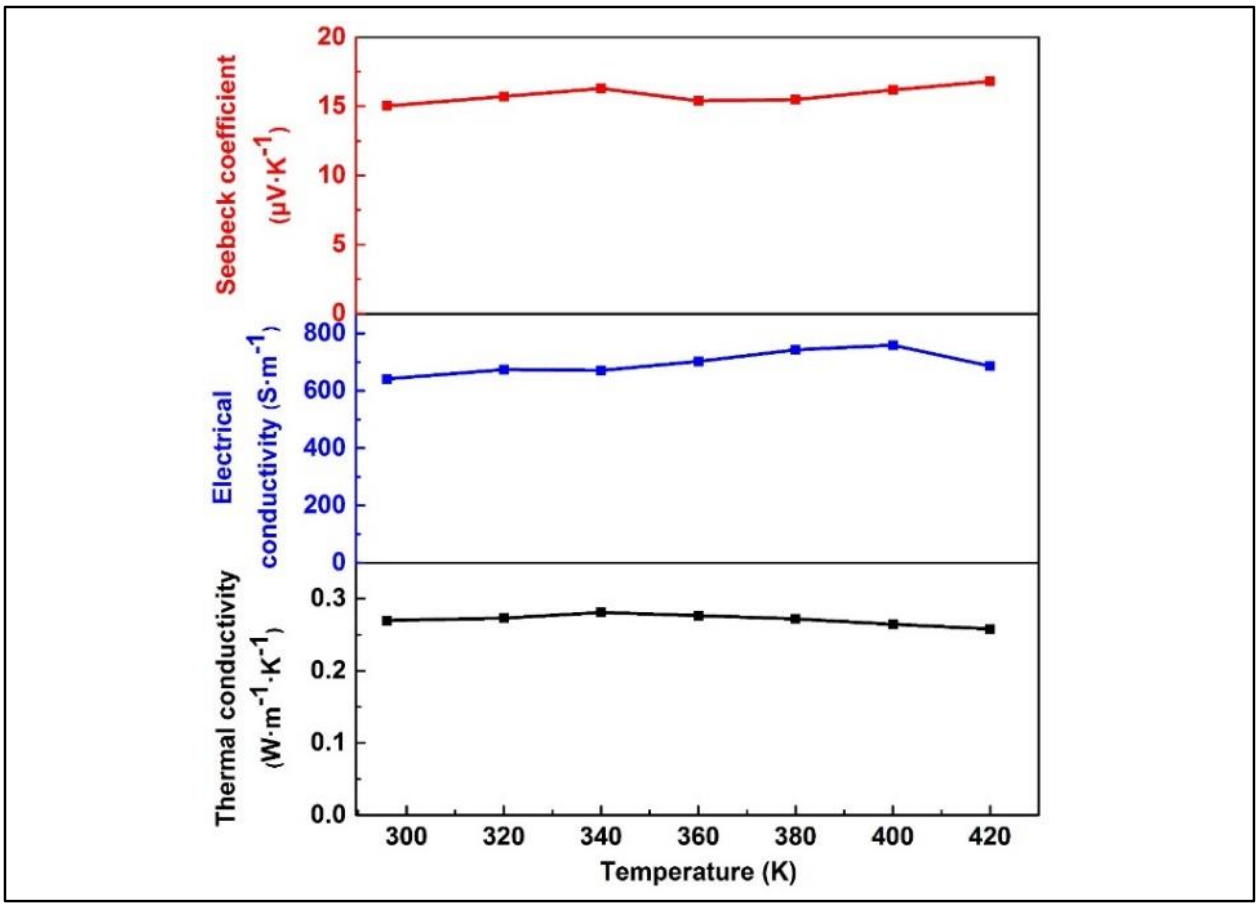

Fig. S5 Properties of the utilized PEDOT: PSS.

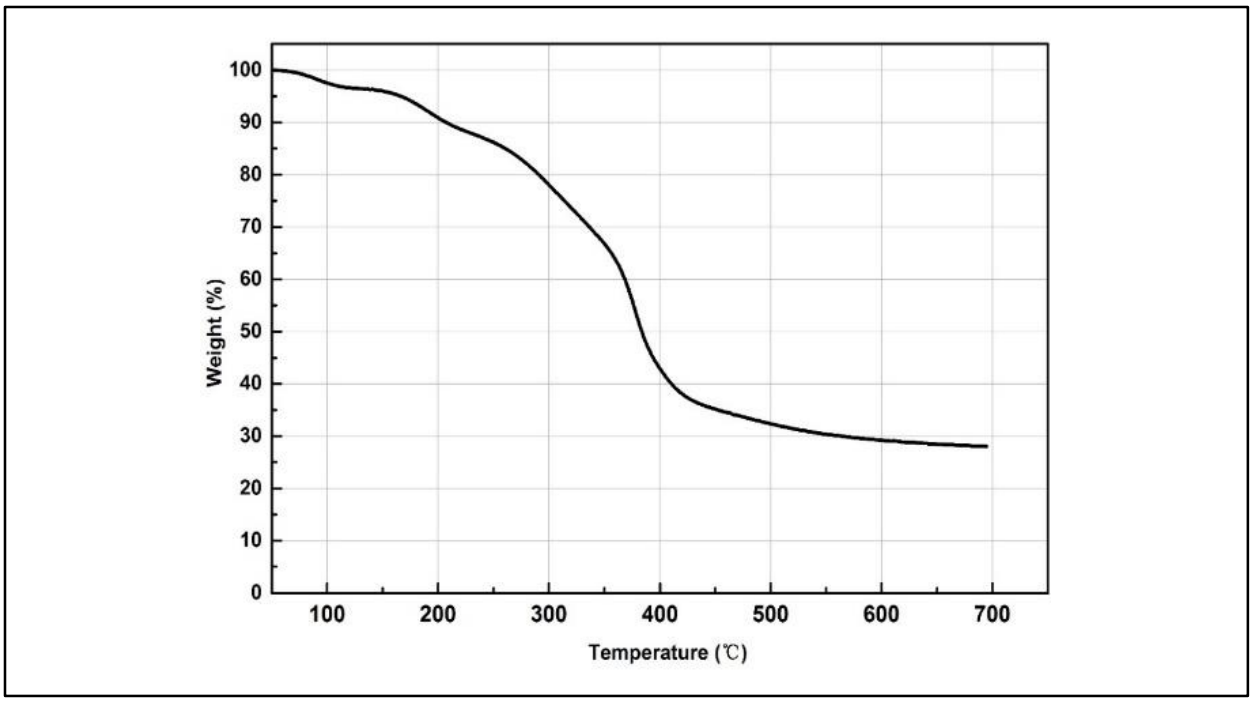

Fig. S6 TGA of the dried PEDOT: PSS

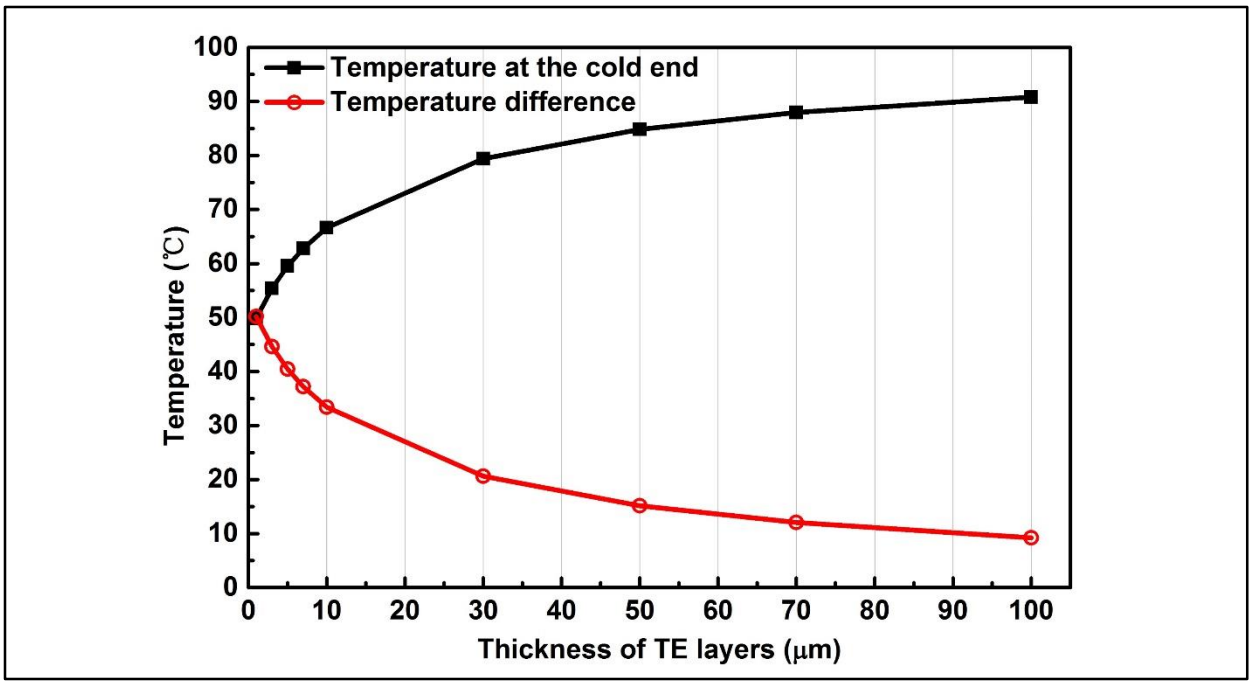

Fig. S7 The relationship between the temperature and the thickness of TE layers.

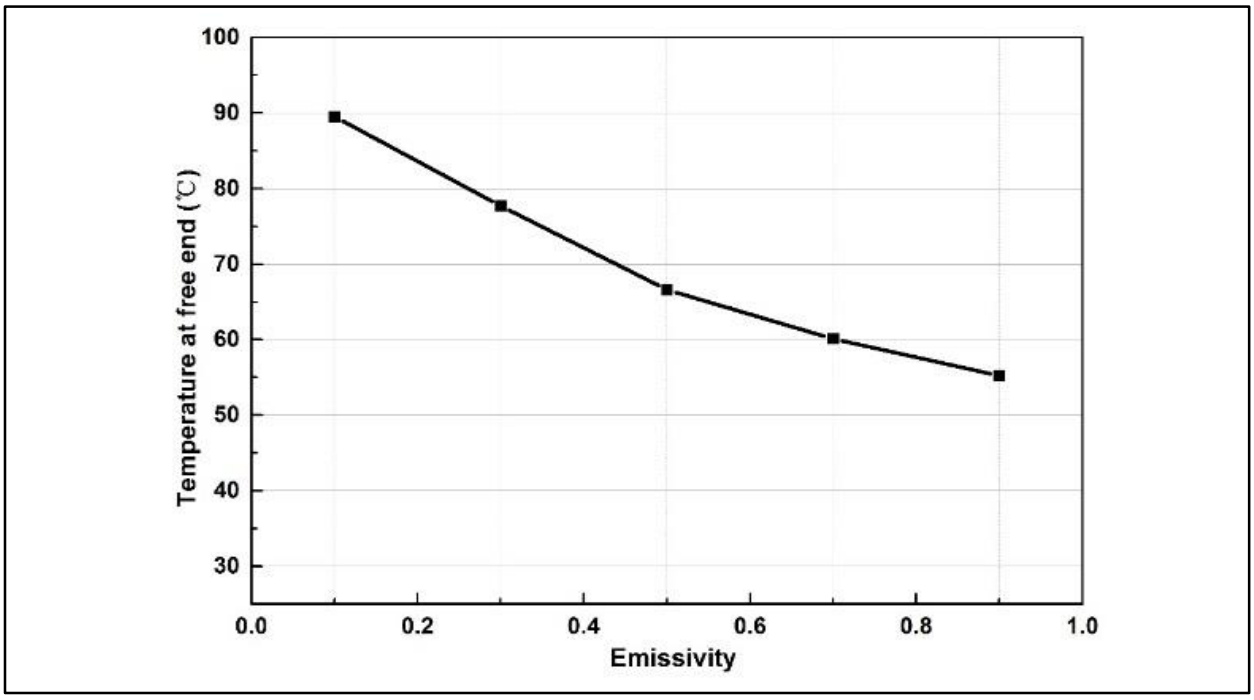

Fig. S8 The temperature at free end for the single 1D FTEG with the fiber radius of 12.5 μm, the length and thickness of TE layer is 1 mm and 10 μm, respectively.

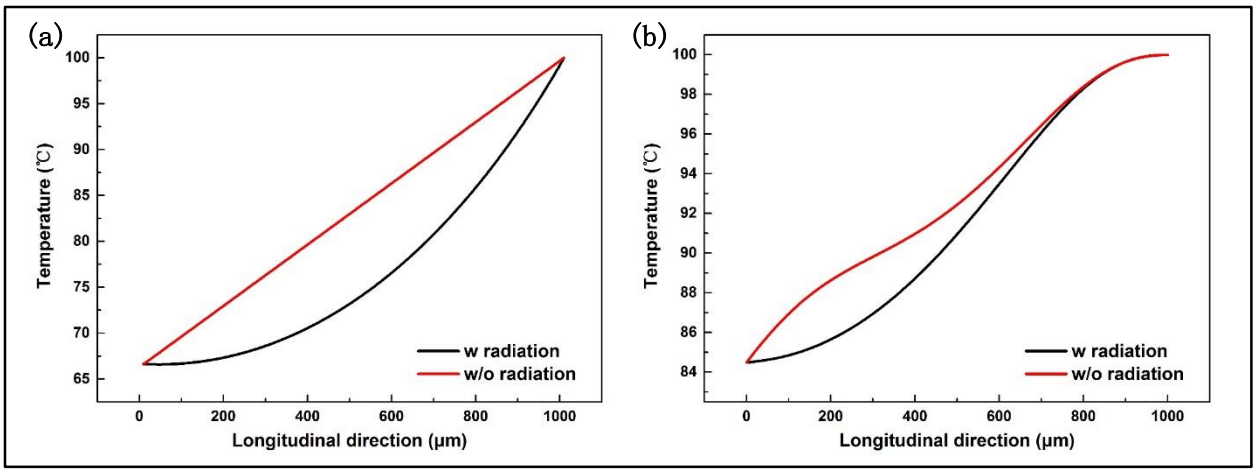

Fig. S9 Temperature distribution of the TE layer along the longitudinal direction of 1D FTEG models: (a) single; (b) array